Reconfigurable RF Receiver Frontends for Multi-Standard Radios

by

Hossein Noori

A thesis submitted to the Graduate Faculty of
Auburn University
in partial fulfillment of the
requirements for the Degree of
Master of Science

Auburn, Alabama
May 9, 2011

Keywords: Reconfigurable Radio, Multi-Standard Radio, Receiver Frontend,
Multiband Radio, Low-Noise Amplifier (LNA), Noise Cancellation

Approved by

Fa Foster Dai, Chair, Professor of Electrical and Computer Engineering
Richard C. Jaeger, Professor of Electrical and Computer Engineering
Bogdan M. Wilamowski, Professor of Electrical and Computer Engineering

Abstract

Several Wireless Communication Standards have been developed over the past few decades to address the growing and varying needs of the users. For example, while cellular access technologies such as GSM and CDMA have satisfied the Wide-Area needs for voice and moderate-speed data communication, the IEEE 802.11 series of standards have satisfied the Local-Area demands for high-speed network access. Furthermore, the ability to establish a Private-Area Network (PAN) has been made possible by the introduction of the Bluetooth standard.

While these and other wireless standards were individually developed and optimized for a specific need, the users expect most, if not all, of them to be incorporated and available to them on a single device; i.e., their handsets. To fulfill this requirement, a new approach to the design of Radio-Frequency (RF) receivers and transmitters shall be adopted in order to accommodate the current and have the capability of handling the future wireless standards.

This document presents the review of current state-of-the-art Multi-Standard Receiver Frontend architectures as well as the Design, Analysis, and Simulation results for a Reconfigurable Multi-standard CMOS Low-Noise Amplifier (LNA) covering the DCS1800, PCS1900, AWS1700, and IMT2100 frequency bands; utilizing positive feedback to improve gain and provide flexibility in input power matching [5], cross-coupling noise cancellation technique [6], and on-chip transistor-based current source. The simulation has been carried out using a 0.12µm CMOS technology and Cadence's Virtuoso Spectre simulation software.

Acknowledgments

I would like to express my sincere gratitude to Dr. Fa Foster Dai, my academic advisor, for his instrumental support and encouragement as well as insightful instructions from the inception to the completion of this work. His directions at various stages of this effort were crucial in overcoming the hurdles and entertaining other ideas for the purpose of enhancement of the design and creation of a fruitful outcome.

I would also like to thank my committee members, Dr. Richard C Jaeger and Dr. Bogdan M. Wilamowski, for their gracious support and discussions.

Finally, I would like to extend a special thank to Mr. Feng Zhao for providing an opportunity for productive technical discussions at various phases of the design.

Table of Contents

List of Tables

List of Figures

List of Abbreviations

AC	Alternating Current
ADC	Analog-to-Digital Converter
AM	Amplitude Modulation
ANT.	Antenna
AWS	Advanced Wireless Services
BiCMOS	Bipolar Complementary Metal-Oxide Semiconductor
BPF	Band-Pass Filter
CDMA	Code-Division Multiple-Access
CMOS	Complementary Metal-Oxide Semiconductor
DC	Direct Current
DCS	Digital Communication System
DVB-H	Digital Video Broadcast - Handheld
E-GSM	Enhanced Global System for Mobile Communications
GPS	Global Positioning System
GSM	Global System for Mobile Communications
HBT	Heterojunction Bipolar Transistor
IEEE	Institute of Electrical and Electronics Engineers
IF	Intermediate Frequency
IM2	Second-order Inter-Modulation
IIP2	Input-referred second-order Intercept Point
IIP3	Input-referred third-order Intercept Point

IMT	International Mobile Telecommunications
I/Q	In-phase/Quadrature-phase
KCL	Kirchhoff's Current Law
KVL	Kirchhoff's Voltage Law
LAN	Local-Area Network
LPF	Low-Pass Filter
LNA	Low-Noise Amplifier
LO	Local Oscillator
MOS	Metal-Oxide Semiconductor
NF	Noise Figure
OpAmp	Operational Amplifier
PAN	Private-Area Network
PCS	Personal Communication System
PLL	Phase-Locked Loop
RF	Radio Frequency
SAW	Surface Acoustic Wave
SDR	Software-Defined Radio
SMD	Surface-Mount Device
UMTS	Universal Mobile Telephone System
VCO	Voltage-Controlled Oscillator
VGA	Variable-Gain Amplifier
WCDMA	Wideband Code-Division Multiple-Access
WiFi	Wireless Fidelity

WiMax Worldwide Interoperability for Microwave Access

WLAN Wireless Local-Area Network

1 Introduction

1.1 Background

The evolution of mobile wireless communication standards over the past three (3) decades has been unimaginable. Almost every technology that has been introduced continues to exist and evolve while new standards are being added. These standards, while some were developed for a specific geographic region, have spread to the rest of the world. For example, CDMA2000 was developed in the USA; however, it enjoys hundreds of millions of subscribers across the world [1]. Similarly, GSM was a trans-European standard; nevertheless, it is currently operational in almost every country in the world [2].

In addition to the multitude of these standards (e.g., Bluetooth, GPS, IEEE 802.11, WiMax, and DVB-H), a given standard generally operates on different frequency bands depending on the country or the region. For example, GSM operates in 900MHz and 1800MHz bands (also known as E-GSM and DCS1800, respectively) in Europe and Asia, while 850MHz and 1900MHz bands (also known as Cellular and PCS1900, respectively) are primarily used in North America. Similarly, the UMTS (WCDMA) operates in the 2.1/1.7GHz (Downlink/Uplink) band (known as AWS1700) in North America while the 2.1/1.9GHz (Downlink/Uplink) band (known as IMT2100) is utilized in the rest of the world.

Figure 1 illustrates the global multi-standard frequency spectrum for wireless communications.

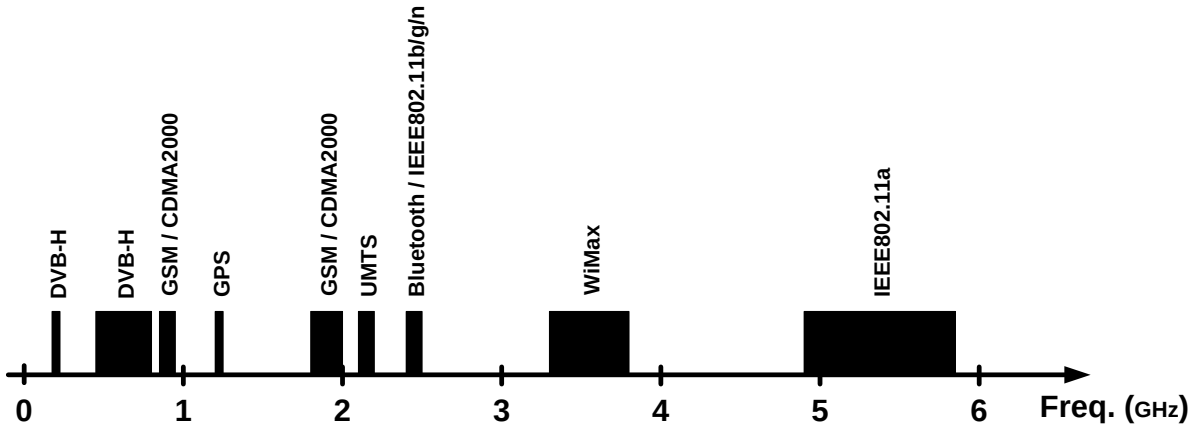

Figure 1. Global Multi-Standard Frequency Spectrum

This amalgamate of standards and their associated frequency spectrums have created an ongoing and increasingly challenging situation for mobile handset manufacturers, as they have to incorporate as many of these standards in their product as possible due to consumer and network operators' demands; the latter arising from the need for seamless and interoperable communication for users in this increasingly mobile world.

Given that the current trend in manufacturing multi-standard mobile handsets does not scale due to utilizing a dedicated chipset for each standard, a new design approach is required that incorporates all wireless standards and frequency bands with maximum sharing of the hardware among the standards in order to minimize the circuit area and power consumption and be feasible for production, hence the need for multi-standard and reconfigurable radio; also known as Software-Defined Radio (SDR).

The design of the receiver and the transmitter of the SDR is very challenging and is currently the subject of on-going research. As such, in this work, we will solely focus on the Receiver Frontend.

1.2 Current Receiver Frontend Design Architectures

Currently, there are two (2) major approaches in the design of the Multi-Standard Receiver Frontend: **1) Narrowband Frontend**, which is the conventional method of handling multiple frequency bands or standards, and **2) Wideband Frontend**, which has become of great interest recently, and several publications have been released to address the challenges associated with the topology.

We will first discuss these two architectures in detail and then present the Reconfigurable Receiver Frontend architecture as a practical approach between the above-mentioned two (2) extremes of the Frontend topology.

1.2.1 Narrowband Receiver Frontend Architecture

Figure 2 illustrates the spectrum selection and circuit architecture for the Multi-Standard Receiver utilizing Narrowband Frontend topology.

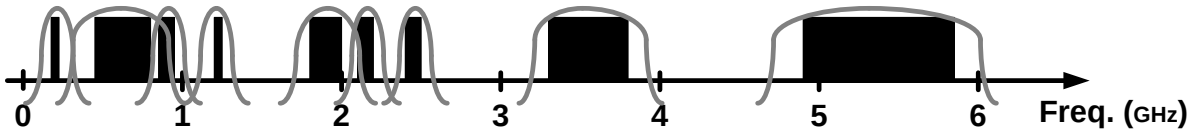

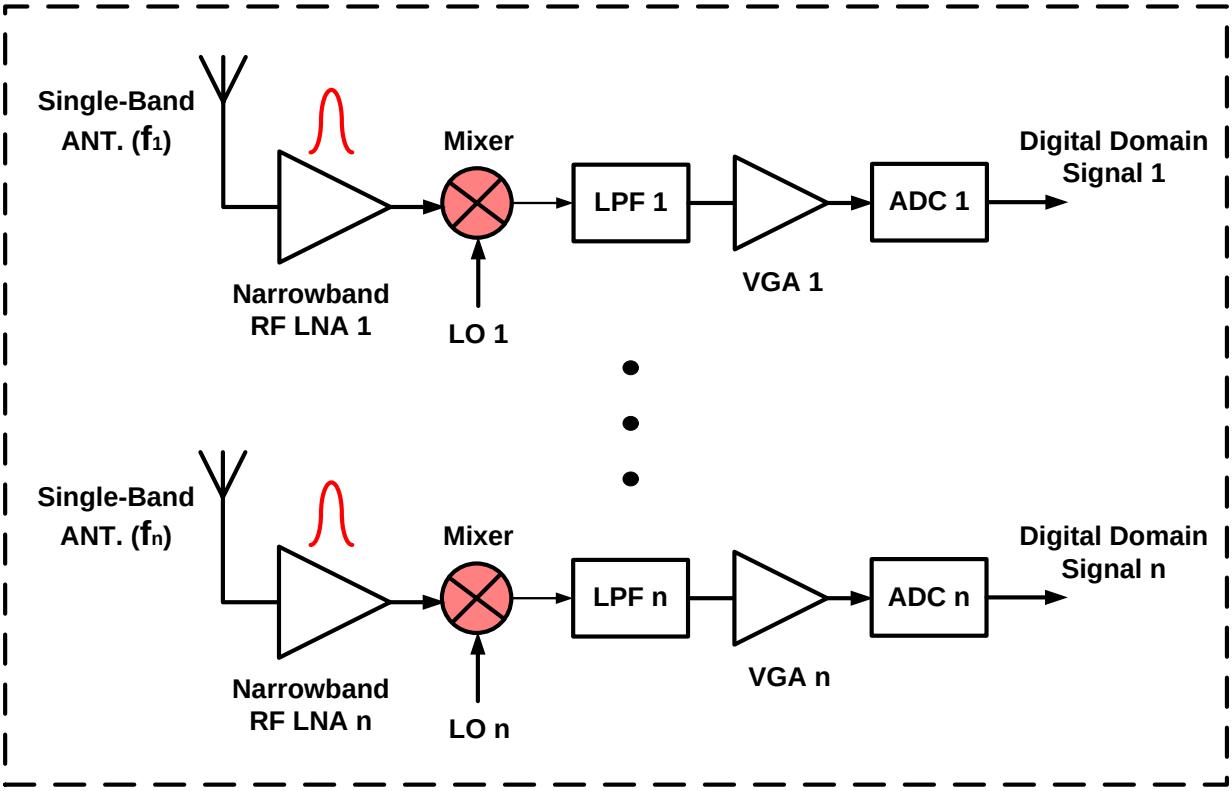

Figure 2. Multi-Standard Frontend using Multiple Narrowband Receivers

As is evident, this type of receiver selects the desired frequency band only [4]. Furthermore, for each frequency band or standard, a dedicated frontend path is utilized. As such, the topology occupies significant silicon die area and is not scalable as more standards are introduced. The Narrowband Receiver Frontend provides frequency selectivity and is immune to out-of-band interference; therefore, it has superior linearity. Furthermore, due to narrow-band input matching requirement, excellent return loss and noise figure may be achieved. Ultimately, this approach consumes less power, as each receiver path is optimized to operate for a specific band.

1.2.2 Wideband Receiver Frontend Architecture

Figure 3 illustrates the spectrum selection and circuit architecture for the Wideband Receiver Frontend, where all wireless standards are simultaneously received and the baseband circuitry selects the desired signal [3], [11], and [12].

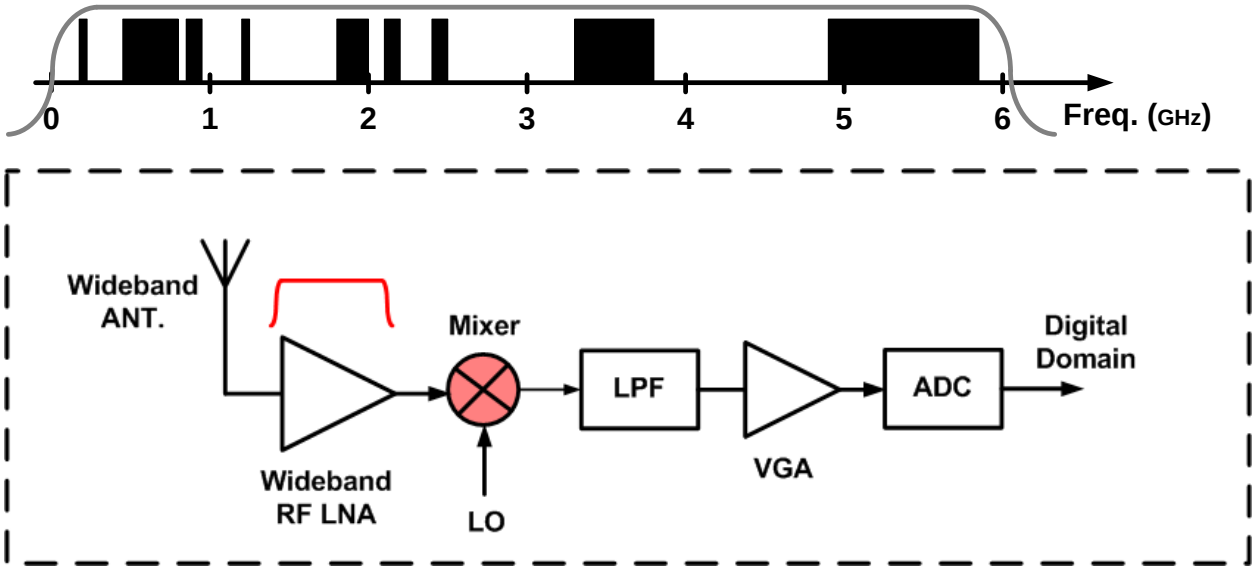

Figure 3. Multi-Standard Frontend using Wideband Receiver Frontend

While the Wideband Receiver Frontend allows concurrent reception of more than one standard, it is not an optimum approach to meet the regulatory requirements of each standard. Furthermore, due to the very wide band of operation, the odd- and even-order inter-modulation products of the desired frequency may fall on other desired frequencies. For example, the third-order inter-modulation products generated by strong DCS1800 or PCS1900 signals may fall on top of the 5GHz WLAN signal [19]. In order to sustain operation in the presence of such blockers, the wideband receiver frontend must have extremely high linearity. The following example from [19] demonstrates the severity of this issue with practical data:

In order to demodulate a 16MHz WLAN signal with a 9dB NF receiver, the input-referred noise floor at 5GHz can be calculated as:

$$Noise\ Floor = -174\frac{dBm}{Hz} + 10\log(16MHz) + 9dB = -93dBm$$

Assuming 0dBm power for the DCS or PCS blocker signal and in order for the third-order inter-modulation product to be below the noise floor, the wideband receiver IIP3 may be calculated as follows:

$$IIP_3 = 0.5 \times \left(3 \times P_{in\_DCS/PCS} - Noise\ Floor\right) = 0.5 \times \left(3 \times 0dBm - (-93dBm)\right)$$

$$= +\mathbf{46.5}\ dBm$$

Obviously, achieving such a high IIP3 is not practical in Integrated Circuits. This simple example demonstrates how critical the issue of out-of-band blockers and consequently high linearity requirement is for the wideband receiver frontend.

Despite the above discouraging statements, the wideband receiver frontend is one of the dominant architectures for the realization of Software-Defined Radio Receiver.

1.3 Reconfigurable Receiver Frontend

The foregoing sections provided the necessary background information for the introduction of Reconfigurable Receiver Frontend. The reader might have concluded by now that the optimum architecture for a multi-standard receiver is neither a wideband nor a narrowband receiver. Indeed, it is an architecture that handles multiple standards while rendering the highest level of integration and hardware sharing and is scalable. We call this architecture a Reconfigurable Receiver Frontend.

Figure 4 illustrates the multi-standard Reconfigurable Receiver Frontend utilizing a single LNA for all homogenous standards.

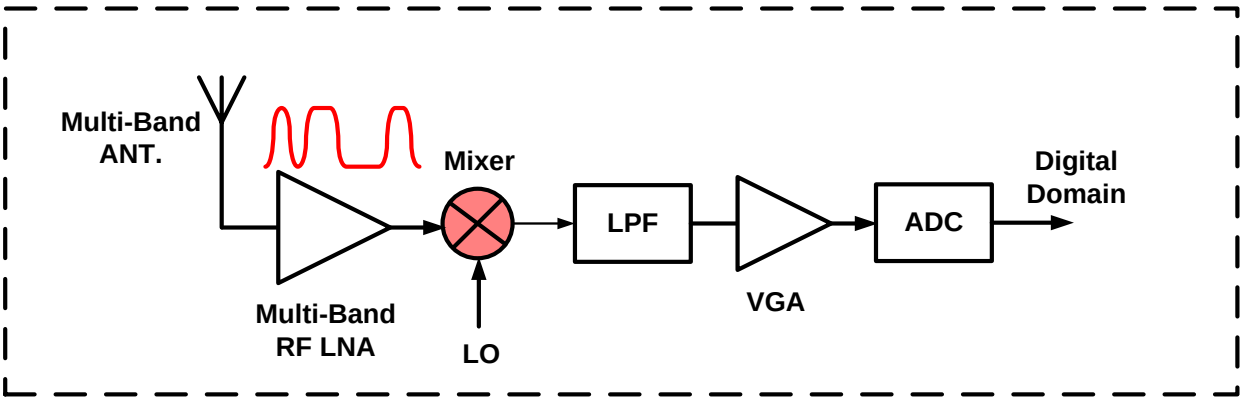

Figure 4. Reconfigurable Receiver Frontend

In this configuration, wireless standards of similar characteristics (e.g., Cellular, E-GSM, DCS1800, PCS1900, and UMTS) are handled by one LNA. Furthermore, the real-world application of the standards plays a major role in the selection of the standards that are accommodated in a single LNA. For example, given that an average user will use at most three (3) standards simultaneously; e.g., being on a cellular call via Bluetooth and surfing the Internet on the WLAN, and that the cellular service shall always be ON due to its priority over other standards, it is reasonable to assume that the Receiver for cellular standards be standalone and dedicated while other standards could share circuitry or be stand-alone, as appropriate.

With the above in mind, this thesis will concentrate on the design, analysis, and simulation of a Reconfigurable Receiver Frontend for the following cellular frequency bands: DCS1800, PCS1900, AWS1700, and IMT2100 by identifying the most appropriate topology published so far [5] and enhancing its performance by incorporating noise cancellation scheme [6], on-chip current source, and reducing the die area by eliminating dedicated inductor for each frequency band. These bands provide global roaming capability for the GSM, CDMA2000, and UMTS (WCDMA) standards.

Table 1 provides information on the spectrum of the above-referenced four (4) cellular Frequency Bands.

Frequency Band	Downlink	Uplink
DCS1800	1805-1880 MHz	1710-1785 MHz
PCS1900	1930-1990 MHz	1850-1910 MHz
AWS1700	2110-2155 MHz	1710-1755 MHz
IMT2100	2110-2170 MHz	1920-1980 MHz

Table 1. Frequency Bands of DCS1800, PCS1900, AWS1700, and IMT2100

As is obvious from this table, the AWS1700 downlink spectrum is confined within that of IMT2100; as such, no additional circuit component is required to accommodate this service; however, for the transmitter, the design will be different, and may require separate circuitry depending on the topology adopted. Furthermore, when referring to IMT2100 in the rest of this document, AWS1700 is also implied.

1.4 Signal Characteristics and Receiver Requirements

Table 2 provides the GSM Signal Characteristics and the E-GSM, DCS1800, and PCS1900 Receiver Specifications as reported in [20]. It shall be noted that these specifications apply to the entire Receiver Frontend (i.e., the LNA and the Mixer combined).

	E-GSM/DCS/PCS Requirement
Channel Bandwidth	200 kHz
Noise Figure	9 dB
IIP3	-18 dBm
IIP2	+49 dBm

Table 2. GSM Signal Characteristics and Receiver Specifications [20]

The stringent second-order Input Intercept Point, IIP2, requirement stems from the AM suppression test as detailed in [21].

Similarly, Table 3 provides the UMTS (WCDMA) Signal Characteristics and the Receiver Specifications as reported in [20] that apply to the entire Receiver Frontend (i.e., the LNA and the Mixer combined).

	UMTS Requirement
Channel Bandwidth	5 MHz
Noise Figure	9 dB
IIP3	-17 dBm
IIP2	+46 dBm

Table 3. UMTS Signal Characteristics and Receiver Specifications [20]

1.5 Organization of the Thesis

The organization of this document is as follows: Section 2 will review the available circuit topologies for Reconfigurable Receiver Frontends, and compare their strengths and weaknesses, and, ultimately, identify the most suitable configuration for the implementation of a practical multi-standard Receiver Frontend.

In Section 3, the existing noise cancellation techniques will be reviewed and the most appropriate circuitry will be identified for incorporation in the proposed Reconfigurable Receiver Frontend architecture.

Section 4 will present the proposed Reconfigurable Receiver Frontend architecture; utilizing the outcome of the evaluations conducted in Sections 2 and 3. Furthermore, the mathematical analysis of the proposed topology will be presented for Gain, Input Matching, and Noise performance.

The simulation results for the proposed Reconfigurable Receiver Frontend will be presented in Section 5. In addition, they will be compared with the closest topology published so far.

Finally, Section 6 will conclude the document and summarize the future work.

2 Available Topologies for Reconfigurable Receiver Frontends

2.1 Low-Noise Amplifier (LNA) Topologies

As the name implies, the Reconfigurable Receiver Frontend is expected to select and amplify a few bands either concurrently [7] (Figure 5) or one-at-a-time.

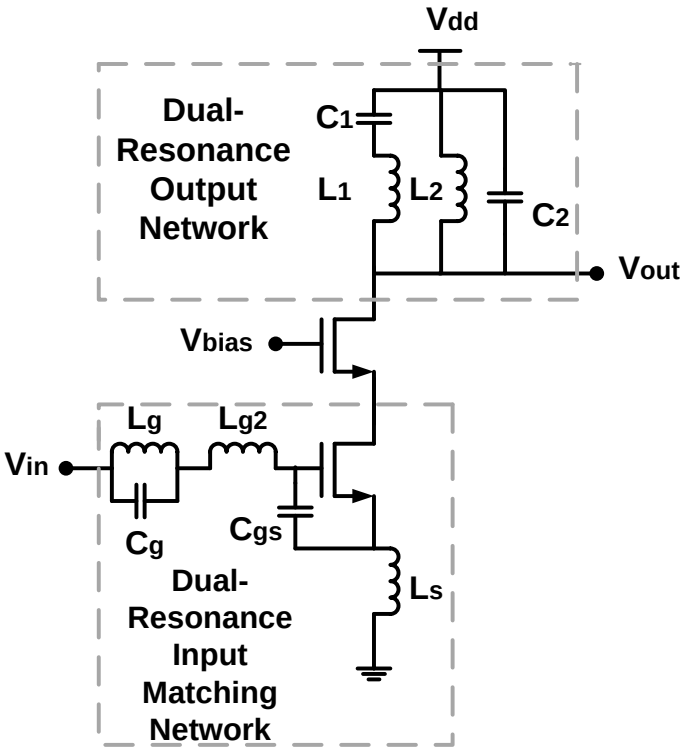

Figure 5. Concurrent dual-band LNA proposed in [7]

The LNA in Figure 5 supports concurrent amplification of the 2.5GHz and 5GHz frequency bands, and the signals may be separated in the baseband for simultaneous processing, depending on the mixer topology adopted [19]. For the low-band operation, L_g (SMD), L_{g2}(Bond-wire), and L_S constitute the input matching network, while for the high-band, the SMD capacitor (C_g) bypasses L_g . At the output, a dual-resonant tank topology is leveraged to provide frequency selectivity and gain for the given band [19].

Considering the fact that, in practice, only one of the frequency bands listed in Table 1 will be active and operational at any given time, concurrent reception and amplification of the frequency bands is neither required nor desired.

For an amplifier to select and amplify a given band, depending on its topology, either both the input and the output terminals (e.g., in Common-Source configuration), or at least the output terminal (i.e., in Common-Gate topology), must be tuned to that band.

2.1.1 Common-Source LNA

In the Common-Source amplifier, there must be a matching network at the input as well as an RLC tank at the output; both resonant at the center frequency of the desired band. Generally, a Source-degeneration inductor as well as one in series with the Gate constitutes the matching network in this topology as depicted in Figure 6.

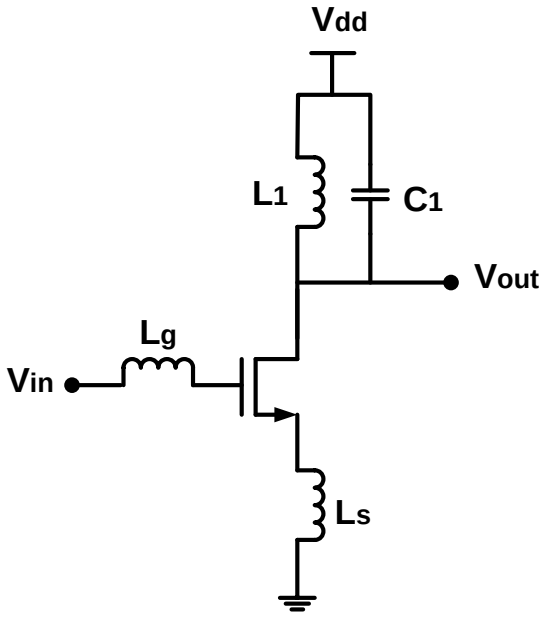

Figure 6. Inductively-Degenerated Tuned Common-Source Amplifier

This topology produces a low-noise configuration, and might seem appropriate for multiband purposes; however, as the number of frequency bands exceeds one (1),

implementation of an input matching network capable of passing multiple bands becomes difficult, if not impractical, as it is narrow-band and not capable of supporting multiband requirements [8]. Furthermore, the frequency alignment of the input matching network and the load tank becomes a major issue due to the variation of the values of L and C caused by the fabrication process. In addition, for every additional band, an inductor must be added to the input matching network, which increases the circuit die area significantly. Finally, using low-Q input matching network to create wideband input will result in increased noise figure of the amplifier. As such, the Common-Source amplifier configuration is not suitable for multiband amplification purposes.

Nevertheless, a wideband version of this amplifier was presented in [22] and illustrated in Figure 7 below.

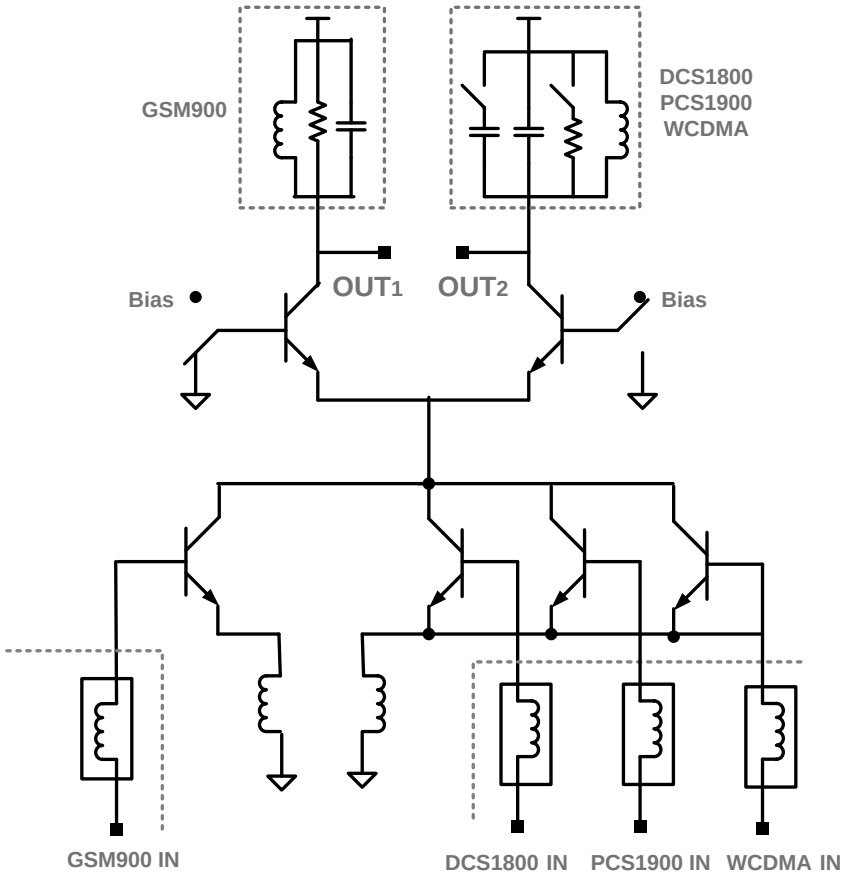

Figure 7. Multi-Standard Inductively-Degenerated LNA

This configuration supports the main cellular standards and frequency bands; i.e., GSM900, DCS1800, PCS1900, and UMTS bands via four (4) dedicated input ports for each spectrum segment. Furthermore, the output is split into two (2) tuned loads to resonate at the low-band GMS900 as well as the high-band DCS/PCS/UMTS. The topology proves to render high performance; however, due to utilization of several inductors (both off-chip and integrated), the configuration is less than desirable to be considered as a scalable candidate for Reconfigurable Receiver Frontend [19].

2.1.2 Common-Gate LNA

In contrast to the inductively-degenerated Common-Source Amplifier, the Common-Gate topology does not require an input matching network (as depicted in Figure 8) due to its wideband input characteristics (limited by input pad capacitance and bond-wire inductance). Nevertheless, input matching is achieved by adjusting the bias current (i.e., g_m) appropriately in order to satisfy the following equation: $R_S = \frac{1}{g_m}$. Furthermore, as will be discussed in Section 2.1.3 and confirmed mathematically in Section 4, employing a feedback network around the Common-Gate amplifier will, in fact, make its input impedance a function of the load impedance; as such, by switching one reactive element in the load tank; i.e., modifying the load tank resonance frequency, the input is also tuned to the desired band without the need for any extra passive component for input matching [13], [14].

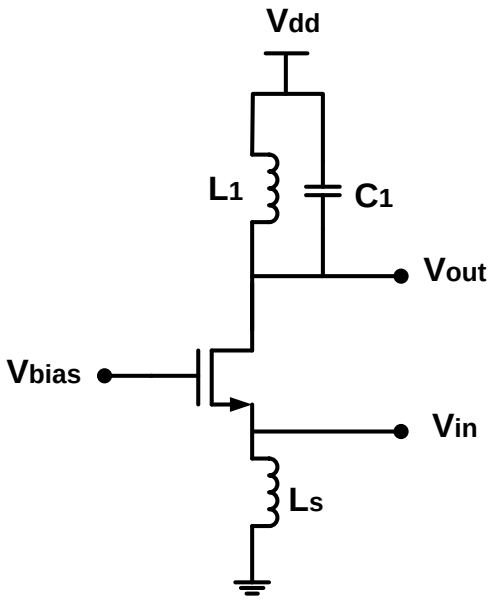

Figure 8. Tuned Common-Gate Amplifier

Before proceeding to the next section, it is worth mentioning that since the frequency bands listed in Table 1 are between 45 MHz and 75 MHz wide, and that these frequency bands

are closely spaced, the tuned amplifier configuration is the most appropriate for the purpose of a implementing a Reconfigurable Receiver Frontend.

2.1.3 Feedback Amplifiers

So far, we have justified the use of the Common-Gate Amplifier as the most appropriate candidate for multiband applications. Furthermore, we have eluded that a feedback network around this configuration results in the input impedance and voltage gain becoming a function of the load; tuning the input impedance and gain frequency responses by switching a single reactive element in the load. Another major characteristic of the feedback network is the enhancement of the linearity; this is due to the high cut-off frequency, f_T , of the sub-micron transistors that makes feedback-based amplifiers a reality for Radio Frequencies. It shall be noted here that the feedback network also improves the noise performance of the amplifier under matching condition [15].

In this section, we will review a few attractive feedback topologies, and adopt the most suitable configuration for our Reconfigurable Receiver Frontend.

2.1.3.1 Negative Voltage-Voltage Feedback LNA

The half-circuit representation of the Negative Voltage-Voltage Feedback LNA proposed by [13] is depicted in Figure 9.

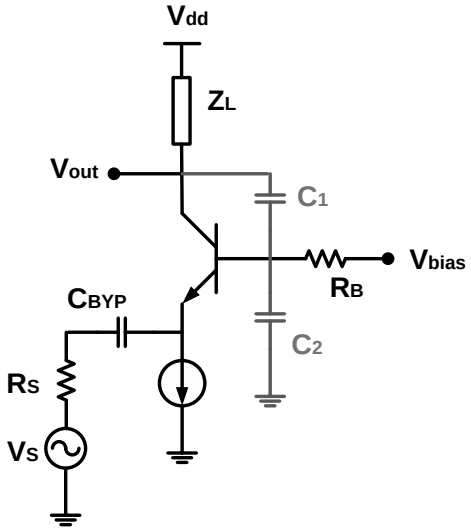

Figure 9. Negative Voltage-Voltage Feedback Topology as proposed in [13]

Although this topology utilizes a Bipolar Transistor, the CMOS-based counterpart is similar. Capacitors C_1 and C_2 constitute the negative Voltage-Voltage feedback network with the feedback factor, $\boldsymbol{\alpha}$, defined as follows:

(1) $$\alpha = \frac{C_1}{C_1+C_2} < 1$$

The capacitive feedback loop provides a degree of freedom in the design. For example, the open-loop input impedance now has a "series" term that is equal to Z_L times the feedback factor ($Z_{in} \approx \frac{1}{g_m} + \alpha Z_L$); as such, the amplifier's trans-conductance, g_m , may now be set much higher in comparison to the Common-Gate topology; resulting in higher DC current and improved Noise Figure and linearity [19] and [4].

As demonstrated in [4], the correlation of the input impedance to the LNA load allows reconfiguration of the amplifier's operating frequency band with negligible noise degradation. In other words, the input impedance and gain ($G_V = \frac{Z_L}{R_S+\frac{1}{g_m}+\alpha Z_L}$) have the same frequency response

as the load impedance, $Z_L(f)$. That is, tuning $Z_L(f)$ results in the alignment of both the gain and the input impedance with the desired frequency band [19].

The differential implementation of this LNA, including the tunable load, is depicted in Figure 10.

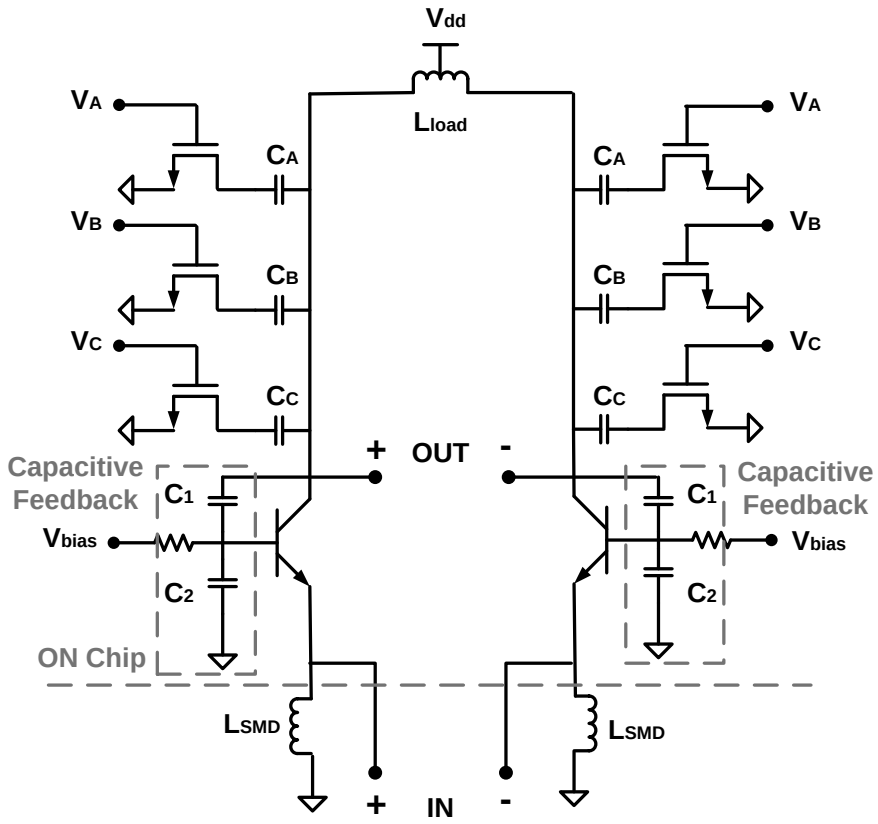

Figure 10. Differential Implementation of the Negative Feedback LNA in [13]

Capacitors C_A, C_B, and C_C, together with the corresponding MOS switches, allow the tuning of the LNA to the desired band. One of the advantages of this topology, as it relates to the load, is that it utilizes a differential inductor, L_{load}, that minimizes the die area and is shared among all frequency bands.

Although this topology is appealing; it suffers from major disadvantages as follows:

1) It utilizes off-chip inductors, L_{SMD}, as the current source. Depending on the frequency band of operation, the off-chip inductor must be large in order not to load the source. Furthermore, it may not be a practical approach at lower frequencies. It is worth mentioning that this specific configuration was implemented for the HiperLAN2/IEEE802.11a frequency bands that operate in the 5GHz range, where an off-chip inductor of 15 nH will produce adequate impedance; however, at our lowest frequency of operation; i.e., DCS1800, larger off-chip inductors are required.

2) Due to the passive nature, and, consequently, less-than-unity feedback factor, the overall gain of the amplifier is degraded. The unity current gain and large parasitic capacitance at the output terminal also contributes to lower gain, as the latter reduces the load impedance at Radio Frequencies.

3) When implemented in pure CMOS, compared to the BiCMOS implementation as performed in [4], the limitations mentioned in 2) become more pronounced, as the amplifier transistor must be large to produce adequate g_m; resulting in additional parasitic capacitance seen by the load.

4) The use of capacitors in parallel with L_{load} for every desired band shall be carried out with caution, as for lower frequencies, larger capacitors will be required, which will degrade the gain as well as the selectivity of the tank. Since the circuit in [13] was designed for 5 GHz range, the tank capacitors were less than 200 fF, and this issue was not pronounced; however, in the case of the frequency bands of interest in this work, a different approach shall be taken to keep these capacitors as small as possible. One approach is to choose as large an inductor as possible to resonate with the transistors' parasitic capacitors at the highest frequency of interest, and

utilize capacitors to resonate with the inductor at the remaining frequency bands. We will employ this latter approach in the architecture of our proposed Multiband LNA

Considering the above disadvantages, this topology does not appear as an appealing candidate for our reconfigurable LNA; nevertheless, its load configuration; i.e., a differential inductor in parallel with switched capacitors is worth considering in the design of a multiband LNA.

2.1.3.2 Positive Voltage-Current Feedback LNA

It was clear from the review of the feedback topology discussed in section 2.1.3.1 that a negative feedback network must be replaced with one that is both non-capacitive (and non-passive, in general) and positive in order to produce a larger-than-unity current gain to overcome the disadvantages mentioned therein.

The half-circuit representation of a Positive Feedback LNA as proposed by [5] is depicted in Figure 11.

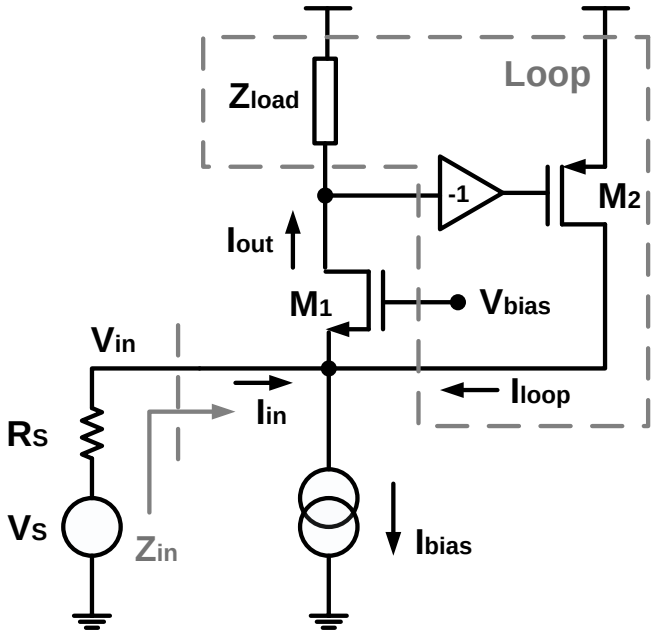

Figure 11. Positive Voltage-Current Feedback Topology as proposed in [5]

In this topology, $Z_{load}(\omega)$ represents the tuned tank impedance; while the amplifier with gain of minus 1 (-1) together with M_2 provide the positive current feedback. The gain of minus 1 is achieved by crossing the drains of the amplifier transistors in the differential configuration as depicted in Figure 12. Furthermore, the feedback factor, $\boldsymbol{\alpha}$, input impedance, and gain are derived as follows:

(2) $$\alpha = g_{\mathrm{m2}}$$

(3) $$Z_{in} = \frac{1}{g_{m1}(1-g_{m2}Z_{load})}$$

(4) $$G_V = \frac{g_{m1}Z_{load}}{1+g_{m1}R_S(1-g_{m2}Z_{load})}$$

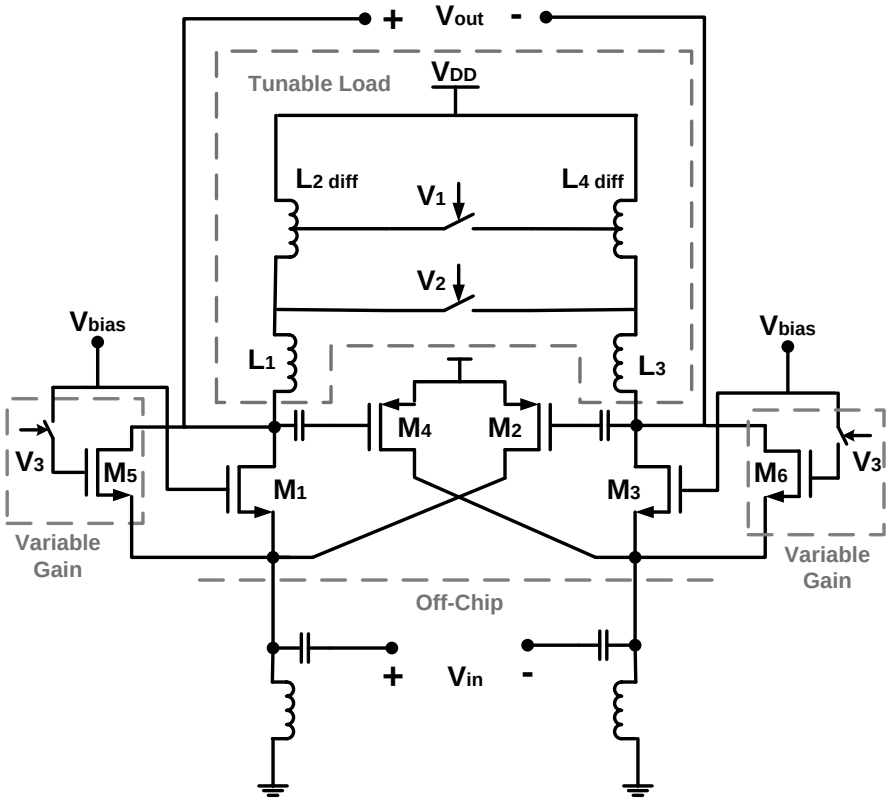

Figure 12. Complete Differential LNA as proposed in [5].

Although this topology addresses some of the major disadvantages of the configuration of Figure 10, it still suffers from the following:

1) The LNA utilizes off-chip inductors as current source, which, similar to the topology depicted in Figure 10, is undesirable, and an approach must be adopted to eliminate it.

2) Given that it is implemented in pure CMOS technology, it has high noise figure compared to that proposed in [13], which utilizes intrinsically-low-noise HBTs. However, it lacks any noise cancellation scheme as evident from the high noise figure reported and provided in Table 7 for comparison.

3) The load tank utilizes so many inductors, which contribute to large die area. The authors of [5] claim that an inductor-only-based load tank provides higher quality factor; however, given the narrow bandwidth of the frequency spectrums of interest in this work, low-value capacitors may be utilized in parallel to a differential inductor, as employed in [13], to provide high-quality-factor load tank.

As will be demonstrated in 4, the advantage of the Positive Feedback LNA is to provide higher than unity current gain; increasing the Transconductance Gain of the amplifier and providing a degree of freedom for input matching.

As such, if the disadvantages mentioned above are addressed and eliminated, this topology may be an acceptable candidate for a reconfigurable LNA.

2.2 Down-Conversion Mixers

2.2.1 Receiver Architectures

Prior to directing our attention to the available down-conversion mixer circuit topologies appropriate for Reconfigurable Receiver Frontend, we shall review the common Receiver Architectures, as they will provide insight into both the suitable receiver architecture for multi-standard applications and the role of down-conversion mixers in the overall receiver configuration.

There are three (3) major classes of Receiver Architectures [25]: 1) Superheterodyne Receiver. 2) Direct Down-Conversion Receiver (also known as Zero IF Receiver), and 3) Low IF Receiver. The following sections will provide a high-level review of these topologies and identify the optimum configuration for reconfigurable receiver frontend.

2.2.1.1 Superheterodyne Receiver

Figure 13 illustrates the Superheterodyne Receiver Architecture [25], where the RF signal received by the antenna is down-converted to baseband using two down-conversion mixers.

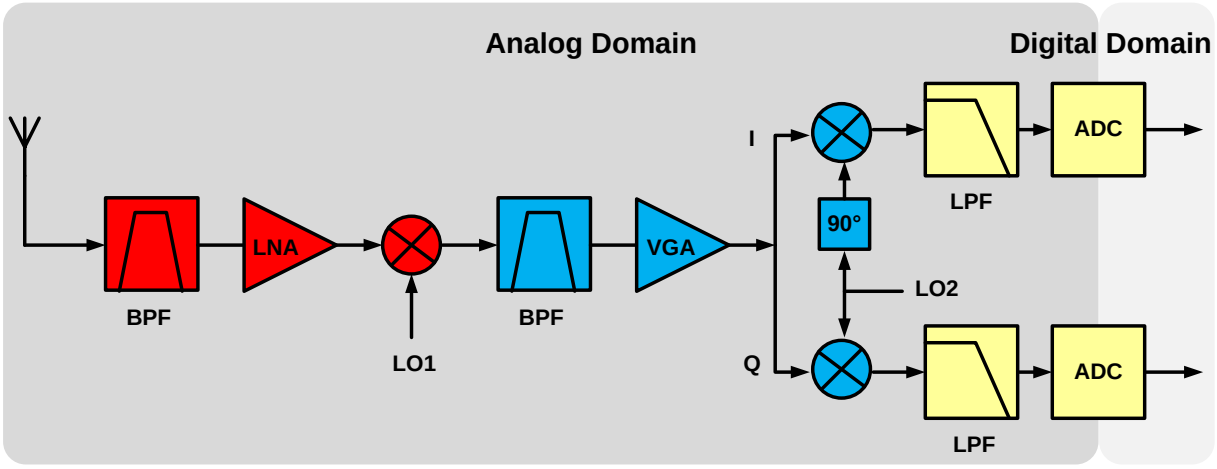

Figure 13. Superheterodyne Receiver Architecture

The first down-conversion occurs from RF to IF; as such, the use of image rejection band-pass filter before the first mixer is necessary. Further, the signal, after filtering and amplification stages, is down-converted from IF to baseband in order to be made available for the ADC and the subsequent digital processing step.

Although the Superheterodyne architecture possesses such advantages as high performance, low power, no DC offset, low design risk, easier design of the LNA and mixer, it suffers from the following disadvantages that render it unsuitable for reconfigurable multi-standard receiver frontend purposes: high cost, the need for two (i.e., for IF and RF) synthesizers,

two mixers, two filters, and external components such as SAW filter. As such, this configuration is not scalable and suffers from poor and low integration.

2.2.1.2 Direct Down-Conversion (Zero IF) Receiver

Figure 14 illustrates the Direct Down-Conversion (Zero IF) Receiver architecture [25], where the RF signal is directly down-converted to baseband (around DC), hence the name Direct Down-Conversion.

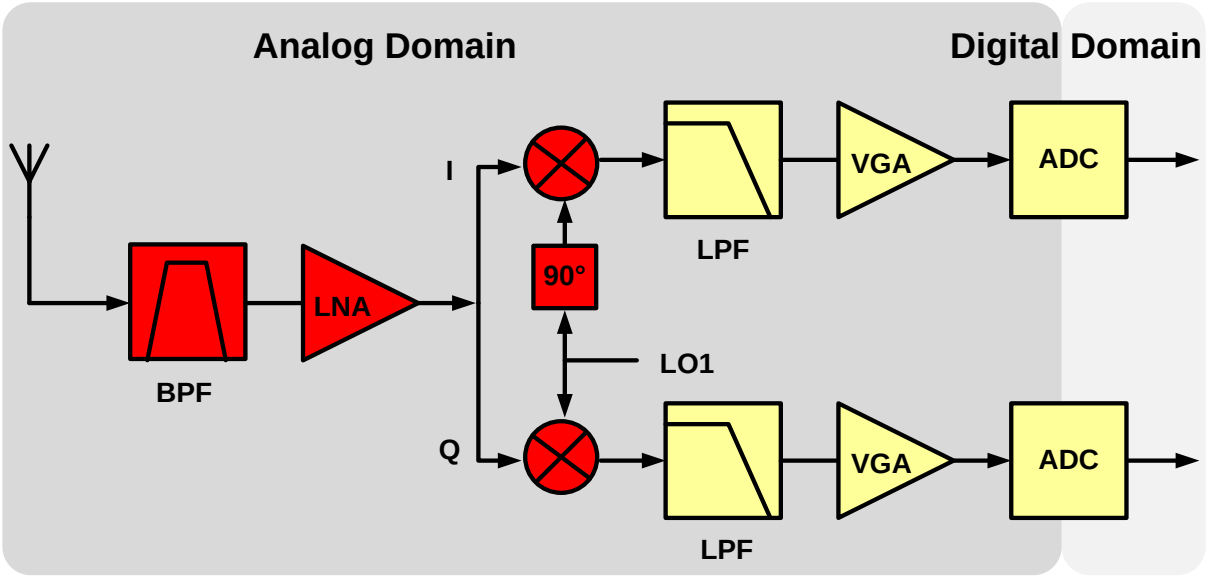

Figure 14. Direct Down-Conversion (Zero IF) Receiver Architecture

The Zero IF receiver architecture benefits from reduced number of components compared to Superheterodyne configuration. This is due to the elimination of the IF SAW filter, the IF PLL, and the image rejection filter. This results in a low-cost receiver topology that enjoys high level of integration. As such, the Zero IF receiver architecture is ideal for reconfigurable receiver frontend purposes.

Nevertheless, the Zero IF configuration suffers from the following disadvantages: On-board Power Amplifier inject locking the VCO, Difficulty in achieving good I/Q quadrature

balance at RF frequencies, LO self-mixing that causes DC offset, AM detection that requires large second-order linearity (IIP2), and flicker noise of the mixer.

It shall be stated that the advantages of the Zero IF architecture overweigh its disadvantages, and has made this topology a widely-used configuration for radio receivers [25]. Also, some of the disadvantages such as DC offset or flicker noise are not so critical for wideband signals; e.g., UMTS (1.92MHz at baseband) or IEEE802.11 (16MHz at baseband).

2.2.1.3 Low IF Receiver

Similar to the Zero IF receiver, the RF signal is down-converted in one stage; however, in order to avoid the DC offset and flicker noise issues, the signal is down-converted to a higher frequency than DC, hence the name Low IF.

The Low IF and Zero IF receiver architectures are identical as far as the analog domain is concerned, except for the bandwidth (cut-off frequency) of the Low-Pass Filter and the performance of the ADC. In the Low IF configuration, the LPF bandwidth is much higher than the signal bandwidth. As such, the ADC must be high-performance and robust in order to digitize a wider band and extract the desired channel.

Clearly, the Low IF topology possesses the same advantages as the Zero IF configuration. However, it is an inevitable architecture for narrow-band signals such as GSM (100 kHz at baseband). Nevertheless, since the analog elements of the Zero- and Low-IF receivers are identical, in the rest of this document, when we refer to Zero IF receiver, the Low IF receiver is also implied if the signal bandwidth is narrow.

2.2.2 Mixer Requirements

Before we proceed to the discussion of the available mixer circuit architectures and their suitability for the Reconfigurable Receiver Frontend, it is prudent to review the circuit-level

requirements for the down-conversion mixer that are derived from the regulatory requirements published by the appropriate standard body as well as the specifications of other components that are a part of the radio and affect the performance of the receiver (e.g., transmitter, duplexer, etc.).

Table 4 provides the Down-Conversion Mixer Requirements for the wireless standards of interest in this work as reported in [19], where the stringent linearity requirements (i.e., IIP2 and IIP3) are obvious.

Standard	Max. Gain	Min. Gain	NF	IIP2	IIP3	BW
GSM	22 dB	0 dB	22 dB	75 dBm	7 dBm	100 kHz
UMTS	18 dB	2 dB	19 dB	70 dBm	10 dBm	1.92 MHz
IEEE 802.11 a/b/g	22 dB	4 dB	22 dB	50 dBm	7 dBm	16 MHz

Table 4. Down-Conversion Mixer Requirements reported in [19]

Depending on the mixer circuit configuration, as will be discussed in the next section, the contributors to the low second- and third-order nonlinearity will be identified and improvement techniques will be discussed.

2.2.3 Mixer Circuits

There are two categories of down-conversion mixers: 1) Active Mixer and 2) Passive Mixer. The Active Mixer consumes power, and provides positive gain. In contrast, the passive mixer does not draw any DC current from the power supply and exhibits negative gain.

In the following sections, we will review the most commonly-used Active and Passive Mixer circuits and their linearity performance.

2.2.3.1 Active Mixer

One of the most widely-used Active Mixer circuits is the conventional Gilbert Cell as illustrated in Figure 15, where the sources of non-linearity are identified [23].

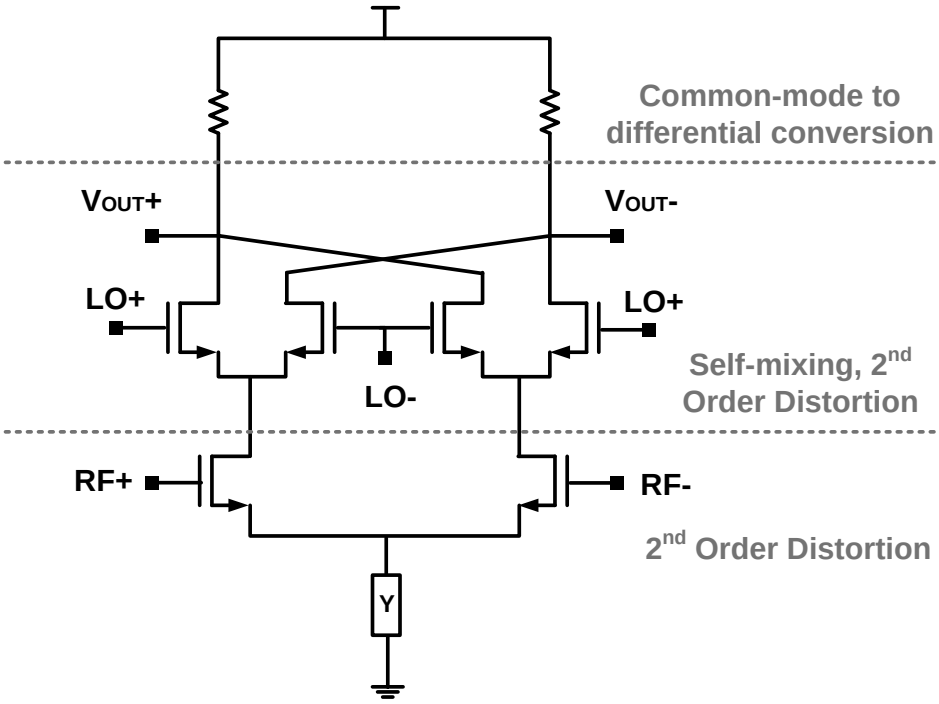

Figure 15. Gilbert Cell [23]

Although the conventional Gilbert cell mixer exhibits IIP2 figure of near +90 dBm at frequencies up to tens of MHz, the IIP2 swiftly declines at GHz frequencies [23]. This is primarily due to the second-order Inter-Modulation distortion contributed by the following phenomena [26]: 1) Self Mixing, 2) Mismatch in Load Resistors, 3) Transconductor nonlinearity, and 4) Switching Pair nonlinearity

The self-mixing occurs as a result of the LO signal being coupled to the RF input and appearing at the source of the Switching Pair and consequently mixing with the LO. Fortunately, layout counter-measures may be utilized to alleviate this issue [23]. For example, by spacing the RF and LO metal tracks as far as possible or, if intersection is unavoidable, crossing them over orthogonally to minimize coupling.

The mismatch in load resistors will result in the conversion of the second-order common-mode components into differential [23]. Fortunately, utilizing highly linear poly-silicon load resistors is a remedy that will maintain the mismatch below 0.1% [23].

It was demonstrated in [26] that the fully differential transconductor configuration provides the highest third-order linearity (i.e., IIP3). As will be seen shortly, other considerations lead to the adoption of a pseudo-differential topology.

The foregoing remedies for second-order IM distortion leave the Switching Pair non-linearity and mismatch as the ultimate limit on the achievable IIP2 [23], which may be explained by referring to Figure 16 adopted from [27].

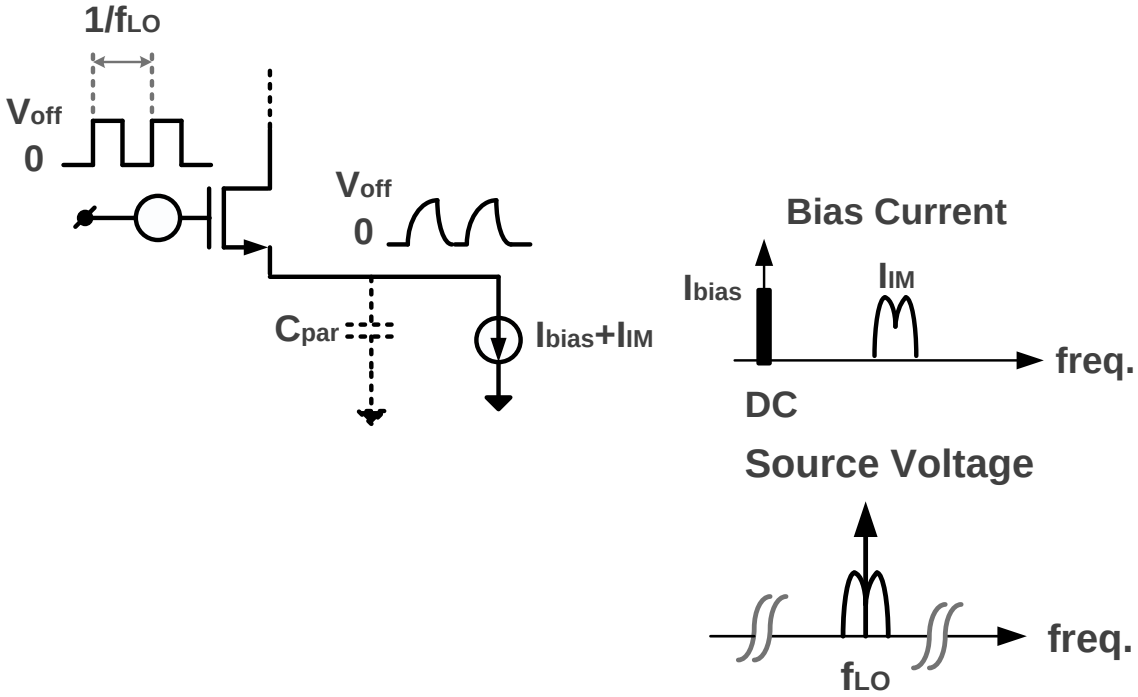

Figure 16. Switching Pair equivalent model for 2nd-order IM Distortion analysis

The mismatch between the switching pair transistors may be modeled as a voltage source referred to as "Offset Voltage" that is in series with the Gate terminal. The Offset Voltage is designated an amplitude of V_{off} and has the same frequency as the LO. Given the large size of

the switching pair transistors to mitigate the flicker noise, the parasitic capacitance seen at the Source terminals (i.e., C_{par}) is significant at RF. Furthermore, the Offset voltage generates a current that is low-pass filtered by C_{par}; creating a baseband replica at the Source terminal. Due to the presence of nonlinearity components in the Bias Current (i.e., I_{IM}), the baseband voltage of the Source terminal is modulated; creating sidebands around I_{IM}. Later, the switching pair downconverts this modulated voltage, and places it over the desired baseband signal; resulting in the corruption of the signal of interest.

So far, we have learned that the non-linearity in the transconductor may be alleviated by utilizing a fully-differential configuration. Furthermore, we just identified the parasitic capacitance at the Source terminal of the switching pairs, C_{par}, to be responsible for its second-order distortion. We will discuss in the following paragraphs the remedies presented by the authors of [23] to address these two issues.

In order to improve the non-linearity of the transconductor, [23] proposes the circuit configuration as illustrated in Figure 17.

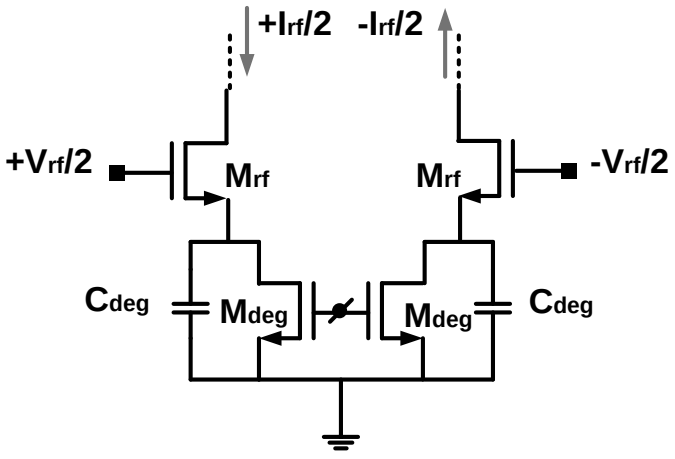

Figure 17. Pseudo-Differential Transconductor to improve linearity [23]

As described in [23], the current source transistor M_{deg} and degeneration capacitor C_{deg} exhibit large impedance at low frequencies; improving the IIP2. However, at RF, C_{deg} bypasses the degeneration transistor M_{deg}, and creates a fully-differential topology that results in improved IIP3.

Since the limiting factor in the case of Switching pair transistors is the parasitic capacitance seen at the Source terminals, one would conclude that employing an inductor in parallel that would resonate at LO frequency would be the logical step to take to address this issue. As a matter of fact, this is exactly the proposed remedy in [23] as illustrated in Figure 18, where inductor L_{SW} resonates with C_{par} at LO frequency.

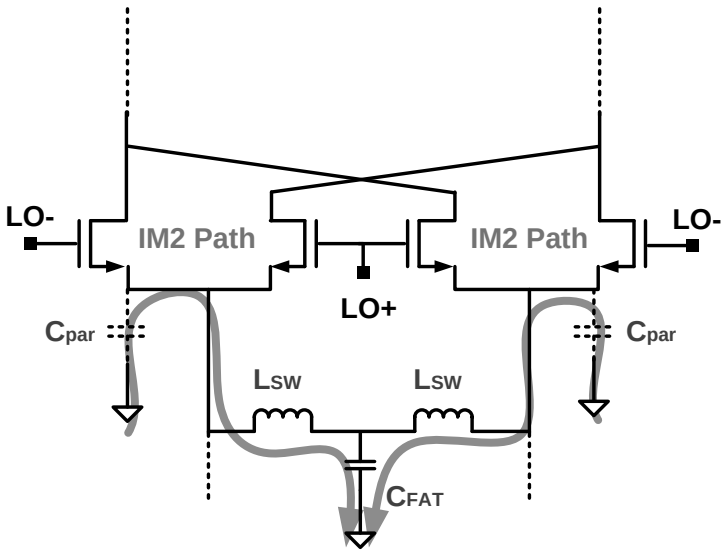

Figure 18. Mitigation of Switching Pair non-linearity [23]

It shall be noted that the authors of [23] have emphasized that the bypass capacitor C_{FAT} has a critical role, and have demonstrated that in its absence, the proposed remedy is ineffective due to the random Offset Voltages of the two Switching pair transistors.

The remedy in Figure 18 improves IIP2 significantly such that the minimum measured IIP2 from 60 samples is +78dBm [23]. Furthermore, the authors claim that a desirable side-effect of this method has been the improvement of the flicker noise.

Although the results reported in [23] are encouraging, the proposed technique for improving the Switching pair non-linearity has the following short-comings: 1) For every wireless standard, a dedicated inductor must be employed; increasing the required silicon area. 2) The proposed method is narrowband in nature. 3) It is an ad-hoc approach. 4) It suffers from the scalability limitations.

2.2.3.2 Passive Mixer

The section on Active Mixer and the limitations associated with its common form of circuit implementation (i.e., Gilbert Cell) demonstrate that an alternative topology must be sought, where such issues are either absent or negligible.

Passive Mixers are an alternative to Active Mixers, and have shown promising performance. The generic topology of the Active Mixer is adopted from [24] and illustrated in Figure 19.

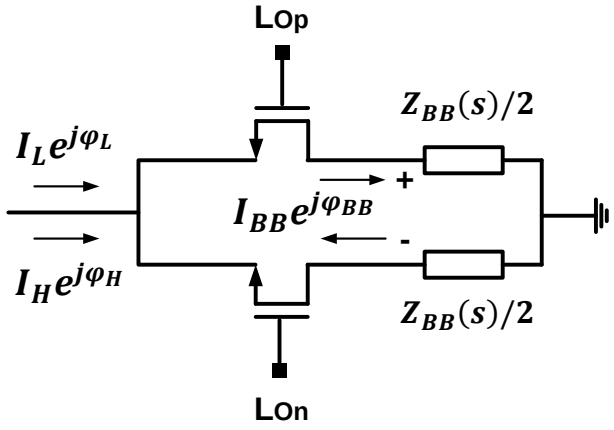

Figure 19. Generic Configuration of Passive Mixer from [24]

In this configuration, the commutating CMOS switches down-convert RF current to baseband current and feed it into baseband impedance Z_{BB}. Since the Passive Mixer commutates RF current only (no DC commutation), it enjoys very low flicker noise at the output [24]. Furthermore, since the voltage swing across the switches is low, the linearity is improved [24].

Figure 20 illustrates one of the most common implementation of the Passive Mixer, where a Common-Gate amplifier is utilized as a current buffer between the switches and the baseband impedance (i.e., the Low-Pass Filter, LPF).

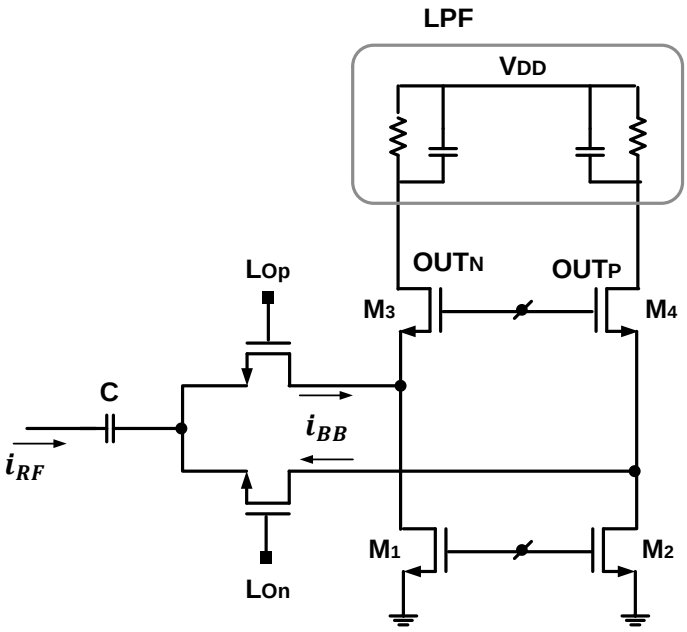

Figure 20. Passive Mixer loaded with Common-Gate Buffer [24]

Another implementation of the Passive Mixer is that illustrated in Figure 21, where the mixer is loaded with OpAmp-based current buffer. The authors of [24] demonstrate that this configuration is superior to that utilizing Common-Gate buffer and that it is ideal for low-voltage applications due to minimal voltage swing across circuit nodes.

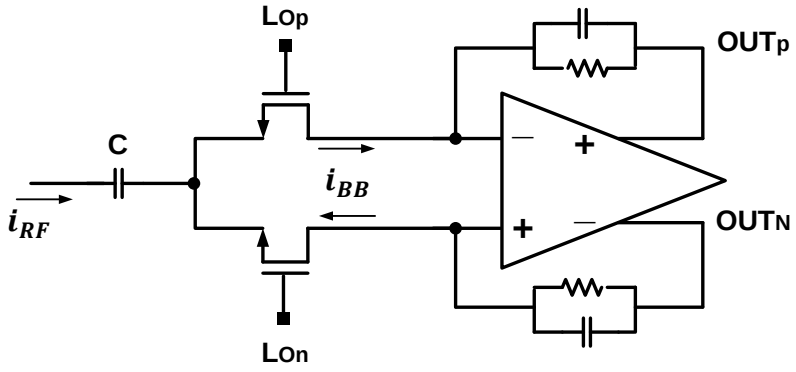

Figure 21. Passive Mixer loaded with OpAmp-based Current Buffer [24]

In the preceding discussion, it has been assumed that the RF current is supplied by the previous stage; e.g., a Transconductor. However, one of the advantages of the passive mixer is that unlike the Gilbert Cell topology, it does not require a dedicated transconductor. As a matter of fact, the LNA that drives the passive mixer acts as the Transconductor as reported in [24] and illustrated in Figure 22.

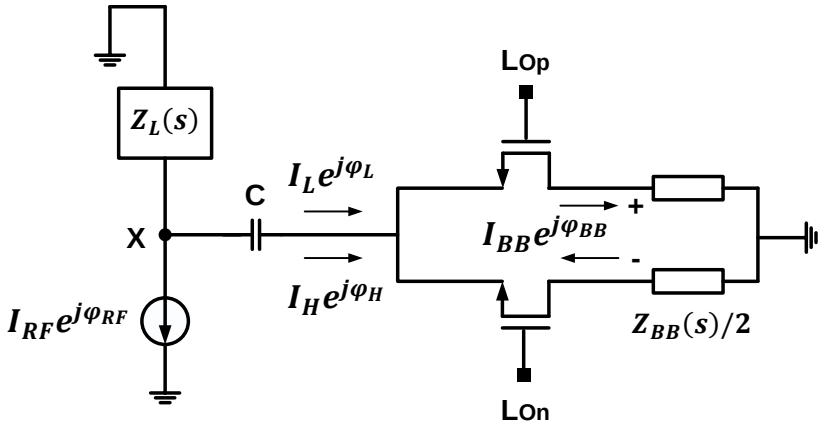

Figure 22. LNA as Transconductor in Passive Mixer [24]

In this figure, the current source represents the LNA and $Z_L(s)$ is the tuned LC tank.

It is prudent at this stage to review the performance of the Passive Mixer as reported in recent publications. [28] has reported IIP2 of +70dBm at the receiver input. Also, IIP3 of +11dBm has been demonstrated by [29]. These encouraging data suggest that the Passive Mixer

shall be considered as the candidate for incorporation in the Reconfigurable Receiver Frontend for Multi-Standard Radios.

3 Available Noise Cancellation Techniques

3.1 Introduction

CMOS-based amplifiers generally exhibit higher noise figure compared to their SiGe-based counterparts [8]. Furthermore, the Common-Gate topology has inferior noise performance compared to that of Common-Source. Ignoring the noise contribution due to the load, the Common-Gate amplifier's minimum Noise Factor is given by [8]:

(5) $$F = 1 + \frac{\gamma}{\alpha}$$

Where γ is the excess channel thermal noise coefficient and $\alpha = \frac{g_m}{g_{d0}}$; with g_{d0} defined as the zero-bias channel conductance.

As such, a method of minimizing the amplifier noise shall be adopted. In this chapter, we will review the available noise cancellation techniques, and adopt the most appropriate topology for our purpose.

3.2 Capacitive Cross-Coupling Noise Cancellation

Figure 23 depicts the Capacitive Cross-Coupling configuration for noise reduction as proposed in [16].

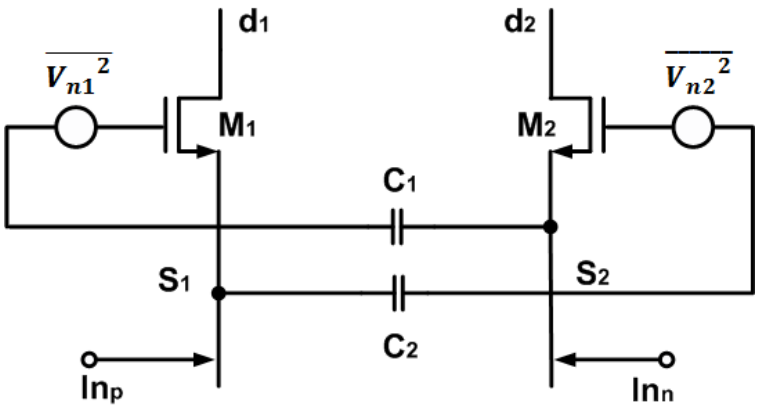

Figure 23. Capacitive Cross-Coupling Technique in [16]

Although the capacitive cross-coupling technique has been used for gain enhancement and matching [17], our interest in this work is its noise performance improvement characteristic.

The capacitive cross-coupling causes the noise of M_1 and M_2 to produce common-mode noise voltages at the output nodes d_1 and d_2.

Considering only the channel thermal noise, the noise factor of the capacitive-coupled transistors M_1 and M_2 is as follows:

(6) $$F = 1 + \frac{\gamma}{2\alpha}$$

Although appealing at the first glance due to number "2" in the denominator, it shall be stated that the authors of [16] utilized the capacitive cross-coupling technique in an LNA with off-chip inductors as current source as depicted in Figure 24.

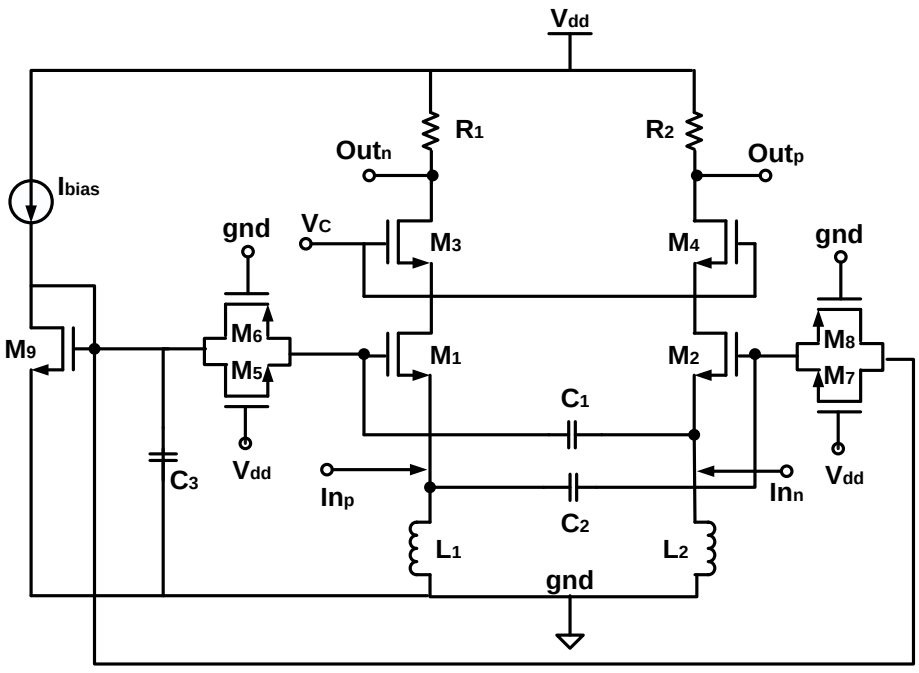

Figure 24. LNA with Capacitive Cross-Coupling in [16]

Since one of the objectives of this work is to eliminate off-chip inductors, the Capacitive Cross-Coupling technique shall be utilized with an on-chip transistor-based current source;

however, as mentioned in [16], the capacitive cross-coupling technique only addresses the noise generated by the amplifier transistors, and does not affect the considerable noise produced by the transistor-based current source. Had the authors utilized on-chip transistor-based current source, the noise factor would have been as follows [3]:

(7) $$F \approx 1 + 1.5\frac{\gamma}{\alpha}$$

Comparing equations (7) and (5), it is apparent that the capacitive cross-coupling technique with on-chip transistor-based current source has inferior noise performance to a pure Common-Gate amplifier.

3.3 Cross-Coupling Noise Cancellation Technique

Another technique in improving the noise performance of the LNA is that proposed in [6] and depicted in Figure 25.

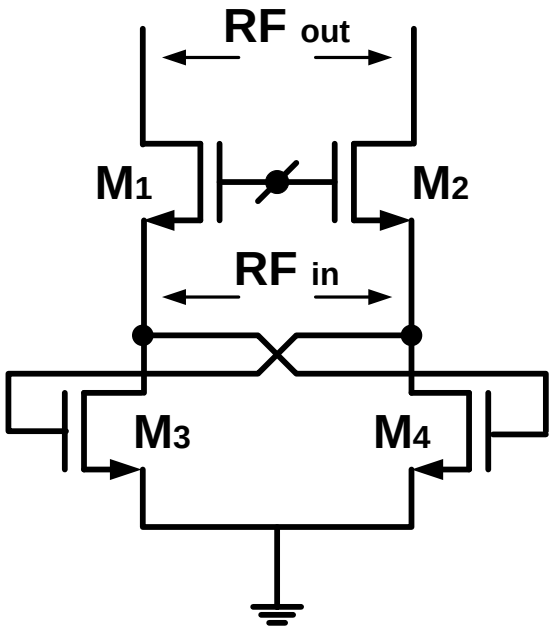

Figure 25. Cross-Coupling Noise Cancellation Technique as employed in [6]

M_3 and M_4 in Figure 25 are responsible for the partial cancellation of the noise of the amplifier transistors M_1 and M_2 as will be demonstrated in Section 4. Furthermore, the introduction of M_3 and M_4 to the circuit topology will provide another degree of freedom in circuit design. It shall be noted that the current source is included but not depicted in Figure 25.

This noise cancellation technique results in the following noise factor equation [6]:

(8) $$F = 1 + 0.657\frac{\gamma}{\alpha}$$

Comparing equations (8) and (7), it is clear that the noise cancellation technique of [6] is superior to that of [16]; as such, we will adopt the configuration illustrated in Figure 25 for our Reconfigurable Receiver Frontend.

4 Proposed LNA Circuit Topology and its Analysis

4.1 Proposed Circuit Topology

The review of the candidate topologies for the LNA and Noise Cancellation techniques in Sections 2 and 3 resulted in the selection of the Positive Feedback LNA of [5], as depicted in Figure 11, and the Noise Cancellation technique of [6], as illustrated in Figure 25. Nevertheless, as discussed in Section 2.1.3.2, the tank load of the LNA of [5] was area-hungry due to the use of multiple inductors, and required an alternative. The alternative load tank was then determined to be the one employed in [13], as it used only one differential inductor and dedicated parallel capacitors for each band of interest; however, it required some modification as discussed in Section 2.1.3.1

Figure 26 depicts the fully-differential representation of the proposed circuit topology for the multiband LNA with positive feedback, noise cancellation circuitry, and on-chip current source for the DSC1800, PCS1900, AWS1700, and IMT2100 frequency bands, where the biasing network is not illustrated for simplicity.

As discussed in section 2.2.3.2, the OpAmp-based Passive Mixer was the most appropriate topology for consideration in the Reconfigurable Receiver Frontend architecture; however, no mixer was included in the simulation efforts of this work; as such, only the LNA section of the Receiver Frontend is illustrated in Figure 26 and will be analyzed and simulated in this and the following sections, respectively.

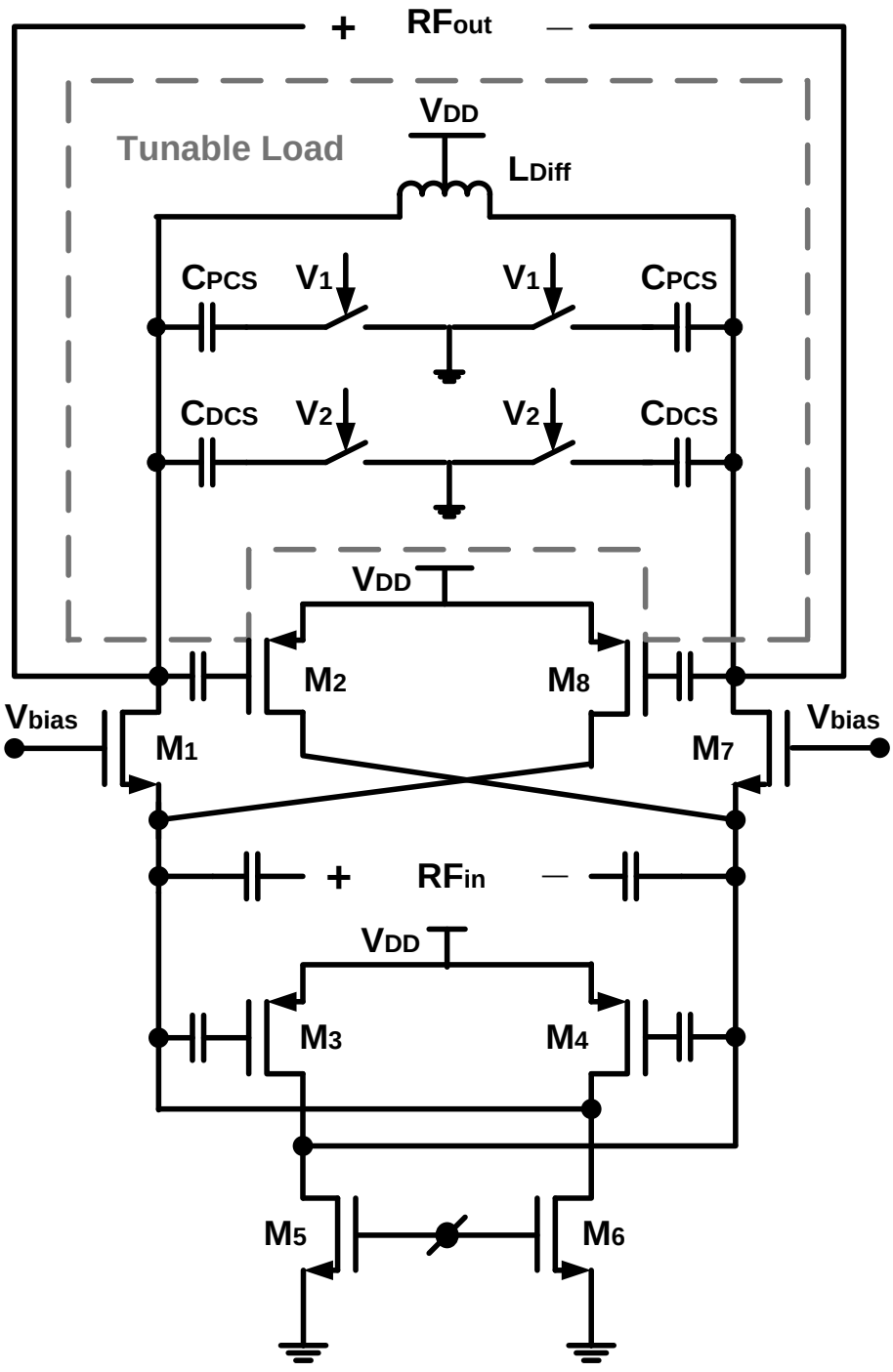

Figure 26. Proposed Multiband LNA Architecture

As discussed in Section 2.1.3.2, unlike the topology in [5], the proposed LNA utilizes on-chip current source and embeds a noise cancellation circuitry adopted from [6]. Furthermore, it

employs only one inductor for all frequency bands of interest. In addition, unlike the load tank proposed in [13], and as discussed in Section 2.1.3.1, one of the bands (i.e., IMT2100) is selected as a result of resonance of the differential inductor with the parasitic capacitance of the amplifier transistors.

The load tank consists of the differential inductor, L_{Diff}, the switchable capacitors, C_{PCS} and C_{DCS}, and the parasitic capacitance of the input transistors.

Inductor L_{Diff} has been sized large enough to resonate with the parasitic capacitance of the input and feedback transistors (M_1 and M_2) at the center frequency of the IMT2100, when the band selection switches are off.

When only the PCS switch is on, Capacitor C_{PCS} resonates with inductor L_{Diff} at the center frequency of the PCS1900 band to select this spectrum.

Similarly, when only the DCS switch is on, a resonance tank consisting of capacitor C_{DCS} and L_{Diff} is created that passes the DCS1800 frequency band.

Since the circuit operates from a 1.2V power supply, and given the large value of the threshold voltage of the NMOS transistors in the 0.12µm technology, PMOS transistors (i.e., M_3 and M_4) have been utilized for cross-coupling purposes.

4.2 Input Matching and Gain

The half-circuit illustration of the proposed circuit topology for the multiband LNA is depicted in Figure 27.

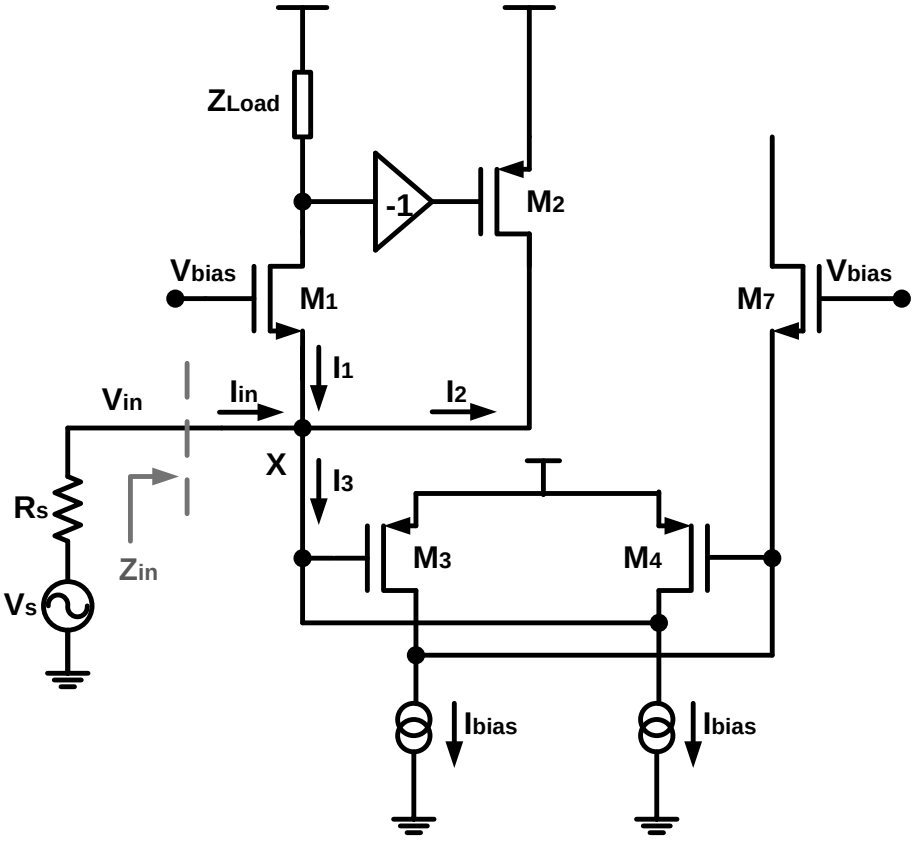

Figure 27. Half-Circuit Topology for the Proposed Multiband LNA

We will use the circuit of Figure 27 for Transconductance Gain and Matching calculations in this section. It shall be noted that currents I_{in} , I_1 , I_2 , and I_3 are AC while I_{bias} is DC. Furthermore, the current sources, as represented by I_{bias}, are on-chip as demonstrated in Figure 26.

The shunt-shunt (voltage-current) positive feedback of Figure 27 has the effect of increasing the input impedance of the simple Common-Gate amplifier as will be demonstrated shortly.

Applying KCL at node X, we obtain the following equation:

(9) $$I_{in} = I_2 + I_3 - I_1$$

Using KVL from the Gate of M_1 to the Source of M_3, we have:

(10) $$V_{gs1} + V_{gs3} = 0$$

Also, from Figure 27, the following may be derived:

(11) $$I_2 = g_{m2} V_{gs2}$$

Where V_{gs2}may be written as follows:

(12) $$V_{gs2} = (-1) \times \left(-I_1 Z_{Load}(\omega)\right) = I_1 Z_{Load}(\omega)$$

However, I_1 is a function of V_{gs1} as shown below

(13) $$I_1 = g_{m1} V_{gs1}$$

Combining (13), (12), and (11), we obtain the following equation for I_2:

(14) $$I_2 = g_{m1} g_{m2} V_{gs1} Z_{Load}(\omega)$$

Assuming the output impedance of the current sources is significantly higher than R_s, we may write I_3 as follows:

(15) $$I_3 = g_{m4} V_{gs4}$$

However, since $g_{m4} = g_{m3}$ and that $V_{gs4} = -V_{gs3}$, I_3 may be re-written as follows:

(16) $$I_3 = -g_{m3} V_{gs3}$$

Combining (10) and (16), we obtain the following equation for I_3 :

(17) $$I_3 = g_{m3} V_{gs1}$$

We are now at a position to derive I_{in} by combining (9), (13), (14), and (17) as follows:

(18) $$I_{in} = (g_{m1} g_{m2} Z_{Load}(\omega) + g_{m3} - g_{m1}) V_{gs1}$$

Also, from Figure 27, it is obvious that

(19) $$V_{in} = -V_{gs1}$$

As such, $Z_{in}(\omega)$ may be derived as follows:

(20) $$Z_{in}(\omega) = \frac{V_{in}}{I_{in}} = \frac{-V_{gs1}}{(g_{m1}g_{m2}Z_{Load}(\omega)+g_{m3}-g_{m1})V_{gs1}}$$

Which may be simplified as follows:

(21) $$Z_{in}(\omega) = \frac{1}{g_{m1}-g_{m3}-g_{m1}g_{m2}Z_{Load}(\omega)}$$

Equation (21) proves the earlier statement on the effect of the positive feedback on increasing the input impedance of the LNA.

Equation (21) also confirms that the input impedance, $Z_{in}(\omega)$, is a function of the load impedance, $Z_{Load}(\omega)$; as such, if $Z_{Load}(\omega)$ is a tunable LC tank, the input impedance will also be tunable and purely resistive at the resonance frequency of the tank (e.g., ω_0).

Assuming the impedance of the load at ω_0 is R_p, the input impedance at the tank resonance frequency may be written as follows:

(22) $$Z_{in}(\omega_0) = \frac{1}{g_{m1}-g_{m3}-g_{m1}g_{m2}R_P}$$

For input matching purposes, we must have $Z_{in}(\omega_0) = R_S$; therefore, the following relationship will hold among circuit parameters at the resonance frequency of the tank.

(23) $$R_s = \frac{1}{g_{m1}-g_{m3}-g_{m1}g_{m2}R_p}$$

Equation (23) confirms that for input matching, there are more degrees of freedom compared to the simple Common-Gate LNA, where $R_s = \frac{1}{g_{m1}}$ must hold.

Nevertheless, as we will see later, g_{m3} will primarily be determined to minimize the noise figure of the LNA.

Another major difference between a simple Common-Gate LNA and that employing Positive-Feedback is concerned with the Transconductance Gain, $G_m = \frac{i_{out}}{V_s}$. In the case of

simple Common Gate amplifier, and under the matching condition, $G_m = \frac{-g_{m1}V_{gs1}}{R_s I_{in} - V_{gs1}} = \frac{-g_{m1}V_{gs1}}{-R_s g_{m1}V_{gs1} - V_{gs1}} = \frac{g_{m1}}{g_{m1}R_s + 1} = \frac{g_{m1}}{2} = \frac{1}{2R_s}$.

However, with the Positive-Feedback topology, G_m may be derived as follows at the resonance frequency of the tank and using Figure 27 as the reference:

(24) $$G_m = \frac{i_{out}}{V_s} = \frac{-I_1}{R_s I_{in} - V_{gs1}}$$

Combining (13), (18), and (24), we have:

(25) $$G_m = \frac{-g_{m1}V_{gs1}}{R_s\left((g_{m1}g_{m2}R_p + g_{m3} - g_{m1})V_{gs1}\right) - V_{gs1}}$$

Which reduces to

(26) $$G_m = \frac{g_{m1}}{1 + R_s(g_{m1} - g_{m3} - g_{m1}g_{m2}R_p)}$$

In matching condition, (23) holds; therefore, G_m is equal to:

(27) $$G_m = \frac{g_{m1}}{2}$$

Unlike the simple Common-Gate topology, where $G_m = \frac{1}{2R_s}$, in the Positive-Feedback topology g_{m1} is not restricted by the source impedance, and may be determined as large as desired to meet the gain requirement. This is another advantage of the Positive-Feedback topology over that of simple common gate.

4.3 Noise Figure

The Common Gate amplifier exhibits worse noise performance than that of Common Source [7]. This is the result of the input matching constraint, which requires the amplifier's g_m to be equal to $\frac{1}{R_s}$; while in the case of Positive-Feedback amplifier, there is a degree of freedom

in the choice of g_m. As such, the noise figure of the Positive-Feedback amplifier may be shown to be close to that of the Inductively-degenerated Common Source amplifier [9].

We will use the half circuit of Figure 28 for the purpose of calculating the Noise Figure of the differential circuit, where only the noise contribution of the bias current sources has been neglected.

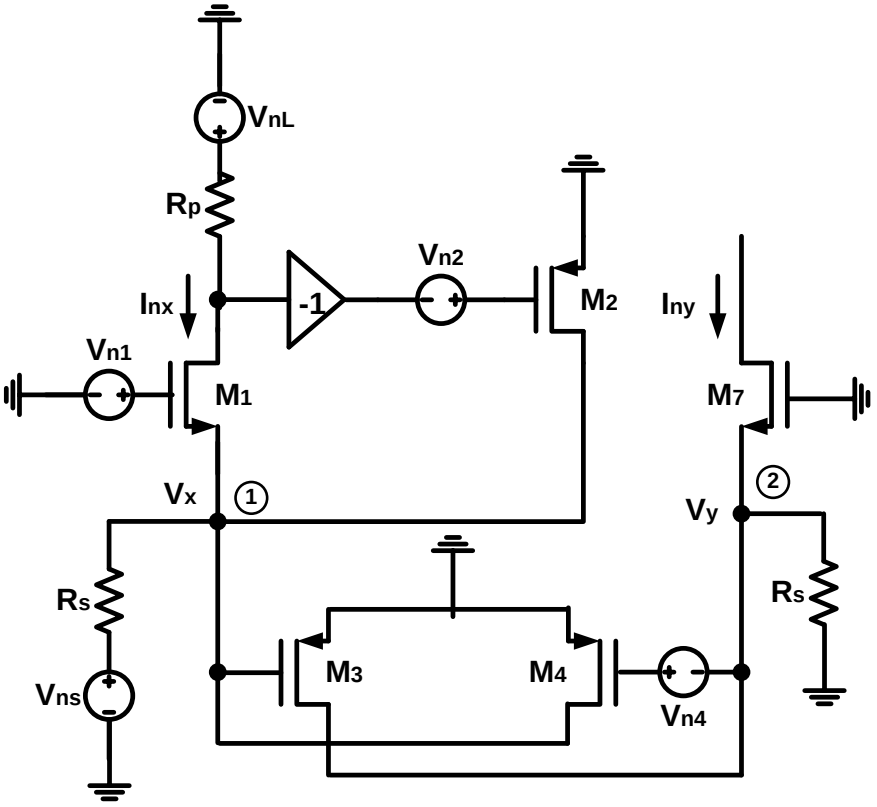

Figure 28. Proposed LNA core for Noise Calculation

Using the lemma proved in [10], we may write each of the noise voltages in Figure 28 as follows:

(28) $$V_{ns}{}^2 = 4KTR_s$$

(29) $$V_{n1}{}^2 = \frac{4KT\gamma_1}{\alpha_1 g_{m1}}$$

(30) $$V_{n2}{}^2 = \frac{4KT\gamma_2}{\alpha_2 g_{m2}}$$

(31) $$V_{n4}{}^2 = \frac{4KT\gamma_4}{\alpha_4 g_{m4}}$$

(32) $$V_{nL}{}^2 = 4KTR_p$$

Where γ is the transistor channel thermal noise and α is a constant defined in Section 3.1.

Applying KCL to node 2, we have

(33) $$g_{m7}(-V_y) = g_{m3}V_x + \frac{V_y}{R_s}$$

Using $g_{m7} = g_{m1}$ and re-organizing (33), we obtain the following equation for V_y :

(34) $$V_y = \frac{-g_{m3}}{g_{m1}+\frac{1}{R_s}}V_x$$

Similarly, by applying KCL to node 2, we have

(35) $$g_{m1}(-V_x) = g_{m2}\left[-\left(-g_{m1}(-V_x)\right)R_p\right] + \frac{V_x - V_{ns}}{R_s} + g_{m4}V_y$$

Using $g_{m4} = g_{m3}$ and re-organizing (35), we obtain the following equation for V_{ns}:

(36) $$V_{ns} = \left(1 + g_{m1}R_s - g_{m1}g_{m2}R_pR_s\right)V_x + g_{m3}R_sV_y$$

Replacing V_y in (36) with its equivalent from (34), and simplifying, we obtain

(37) $$V_{ns} = \frac{2g_{m1}R_s+1+g_{m1}{}^2R_s{}^2-g_{m1}g_{m2}R_pR_s(g_{m1}R_s+1)-g_{m3}{}^2R_s{}^2}{g_{m1}R_s+1}V_x$$

Consequently, V_x may be written as a function of V_{ns} as follows:

(38) $$V_x = \frac{1+g_{m1}R_s}{1+2g_{m1}R_s+R_s{}^2(g_{m1}{}^2-g_{m3}{}^2)-g_{m1}g_{m2}R_pR_s(1+g_{m1}R_s)}V_{ns}$$

Incorporating (38) in (34), we obtain the following equation for V_y as a function of V_{ns} :

(39) $$V_y = \frac{-g_{m3}R_s}{1+2g_{m1}R_s+R_s{}^2(g_{m1}{}^2-g_{m3}{}^2)-g_{m1}g_{m2}R_pR_s(1+g_{m1}R_s)}V_{ns}$$

In order to calculate the two output currents I_{nx} and I_{ny} due to V_{ns}, we use the following equations:

(40) $$I_{nx} = -g_{m1}V_x$$

And

(41) $$I_{ny} = -g_{m1}V_y$$

Replacing V_x in (40) with its equivalent from (38) and V_y in (41) with its equivalent from (39), we have

(42) $$I_{nx} = \frac{-g_{m1}(1+g_{m1}R_s)}{1+2g_{m1}R_s+{R_s}^2({g_{m1}}^2-{g_{m3}}^2)-g_{m1}g_{m2}R_pR_s(1+g_{m1}R_s)}V_{ns}$$

And

(43) $$I_{ny} = \frac{g_{m1}g_{m3}R_s}{1+2g_{m1}R_s+{R_s}^2({g_{m1}}^2-{g_{m3}}^2)-g_{m1}g_{m2}R_pR_s(1+g_{m1}R_s)}V_{ns}$$

Finally, using the equation ${I_{ns\_diff}}^2 = \left|I_{nx} - I_{ny}\right|^2$, where ${I_{ns\_diff}}^2$ represents the differential output noise power due to source impedance noise voltage (i.e., V_{ns}), we have

(44) $${I_{ns\_diff}}^2 = \left|\frac{g_{m1}(1+g_{m1}R_s+g_{m3}R_s)}{1+2g_{m1}R_s+{R_s}^2({g_{m1}}^2-{g_{m3}}^2)-g_{m1}g_{m2}R_pR_s(1+g_{m1}R_s)}V_{ns}\right|^2$$

Following similar steps for the other noise sources as depicted in Figure 28, we obtain the following differential output noise power equations:

(45) $${I_{n1\_diff}}^2 = \left|\frac{g_{m1}\left(1+g_{m1}R_s-{g_{m3}}^2{R_s}^2-g_{m1}g_{m3}{R_s}^2(1-g_{m2}R_p)\right)}{1+2g_{m1}R_s+{R_s}^2({g_{m1}}^2-{g_{m3}}^2)-g_{m1}g_{m2}R_pR_s(1+g_{m1}R_s)}V_{n1}\right|^2$$

(46) $${I_{n4\_diff}}^2 = \left|\frac{g_{m1}g_{m3}R_s(1+g_{m1}R_s+g_{m3}R_s)}{1+2g_{m1}R_s+{R_s}^2({g_{m1}}^2-{g_{m3}}^2)-g_{m1}g_{m2}R_pR_s(1+g_{m1}R_s)}V_{n4}\right|^2$$

(47) $${I_{n2\_diff}}^2 = \left|\frac{g_{m1}g_{m2}R_s(1+g_{m1}R_s+g_{m3}R_s)}{1+2g_{m1}R_s+{R_s}^2({g_{m1}}^2-{g_{m3}}^2)-g_{m1}g_{m2}R_pR_s(1+g_{m1}R_s)}V_{n2}\right|^2$$

(48) $${I_{nL\_diff}}^2 = \frac{4KT}{R_p}$$

Where ${I_{n1\_diff}}^2$, ${I_{n4\_diff}}^2$, ${I_{n2\_diff}}^2$, and ${I_{nL\_diff}}^2$ are the noise power due to transistor M_1, transistor M_4, transistor M_2, and load R_p, respectively.

We are now equipped with the necessary data to calculate the Noise Figure of the differential LNA using the following equation:

(49) $$F = \frac{2I_{ns\_diff}{}^2 + 2I_{n1\_diff}{}^2 + 2I_{n2\_diff}{}^2 + 2I_{n4\_diff}{}^2 + 2I_{nL\_diff}{}^2}{2I_{ns\_diff}{}^2}$$

Assuming $\gamma_1 = \gamma_2 = \gamma_4 = \gamma$ and $\alpha_1 = \alpha_2 = \alpha_4 = \alpha$ and substituting in (49) the noise power calculated in (44), (45), (46), (47), and (48), and replacing V_{ns}, V_{n1}, V_{n2}, and V_{n4} with their equivalent from (28), (29), (30), and (31), we obtain the following equation for the Noise Figure:

(50) $$F = 1 + \frac{\gamma}{\alpha} g_{m2} R_s + \frac{\gamma}{\alpha} g_{m3} R_s + \left(\frac{\gamma}{\alpha}\right) \frac{\left[1 + g_{m1} R_s - g_{m3}{}^2 R_s{}^2 - g_{m1} g_{m3} R_s{}^2 (1 - g_{m2} R_p)\right]^2}{g_{m1} R_s (1 + g_{m1} R_s + g_{m3} R_s)^2} +$$

$$\frac{\left[1 + 2g_{m1} R_s + R_s{}^2 (g_{m1}{}^2 - g_{m3}{}^2) - g_{m1} g_{m2} R_p R_s (1 + g_{m1} R_s)\right]^2}{g_{m1}{}^2 R_s R_p (1 + g_{m1} R_s + g_{m3} R_s)^2}$$

Where the second, third, fourth, and the fifth terms represent the noise contribution from transistor M_2, transistor M_4, transistor M_1, and the load, respectively.

Equation (50) clearly demonstrates that transistor M_4 reduces the noise contribution of transistor M_1 and the load R_p as evidenced by the terms $-g_{m3}$ and $+g_{m3}$ terms in the numerator and denominators, respectively, of the fourth and the fifth terms. However, this noise reduction characteristic of M_4will be limited to the value of g_{m3} that is less than a certain number, beyond which, due to the third term (i.e., $\frac{\gamma}{\alpha} g_{m3} R_s$), M_4 will start degrading the noise figure.

Equation (50) may be further simplified by substituting $g_{m2} R_p$ with its equivalent in matching condition from (23). Therefore, in matching condition, (50) reduces to the following:

(51) $$F = 1 + \frac{\gamma}{\alpha} g_{m2} R_s + \frac{\gamma}{\alpha} g_{m3} R_s + \left(\frac{\gamma}{\alpha}\right) \frac{\left[1+(g_{m1}-g_{m3})R_s - 2{g_{m3}}^2 {R_s}^2\right]^2}{g_{m1} R_s (1+g_{m1}R_s+g_{m3}R_s)^2} + \frac{[2(1+g_{m1}R_s)+g_{m3}R_s(1+g_{m1}R_s-g_{m3}R_s)]^2}{{g_{m1}}^2 R_s R_p (1+g_{m1}R_s+g_{m3}R_s)^2}$$

Equation (51) more clearly demonstrates the noise cancellation effect of M_4; however, due to the complexity of the interaction among the parameters listed in (51), the optimum value for g_{m3} may not be obtained analytically; as such, for a given gain requirement (i.e., g_{m1}), the simulation tool will be utilized to achieve the lowest possible g_{m3} . Furthermore, this equation reveals that for improved noise performance, g_{m1} must be maximized reasonably, as permitted by design and fabrication limitation.

4.4 LNA Design Parameters

The insight and the mathematical derivations obtained in Sections 4.2 and 4.3 provide for the determination of design parameters for Gain, Matching, and Noise Performance.

Although equations (27) and (51) suggest that higher g_{m1} results in larger G_m and lower noise figure, respectively, the achievable value for g_{m1} is restricted by current consumption, power supply voltage, device characteristics, and the die area limitations. As such, in this design, attempt was made to maximize g_{m1}while maintaining reasonable power consumption and device size. Table 5 illustrates the optimum device parameters that were achieved from the simulation of the circuit in Figure 26.

Parameter	Optimum Value
g_{m1}	49.2 mS
g_{m2}	0.645 mS
g_{m3}	3.6 mS

Table 5. Optimum Device Parameters obtained from simulation

5 Simulation Results

5.1 Gain, Matching, and Isolation

5.1.1 Conversion Gain

Figure 29 and Figure 30 depict plots of the Conversion Gain of the proposed circuit topology for all three (3) frequency bands.

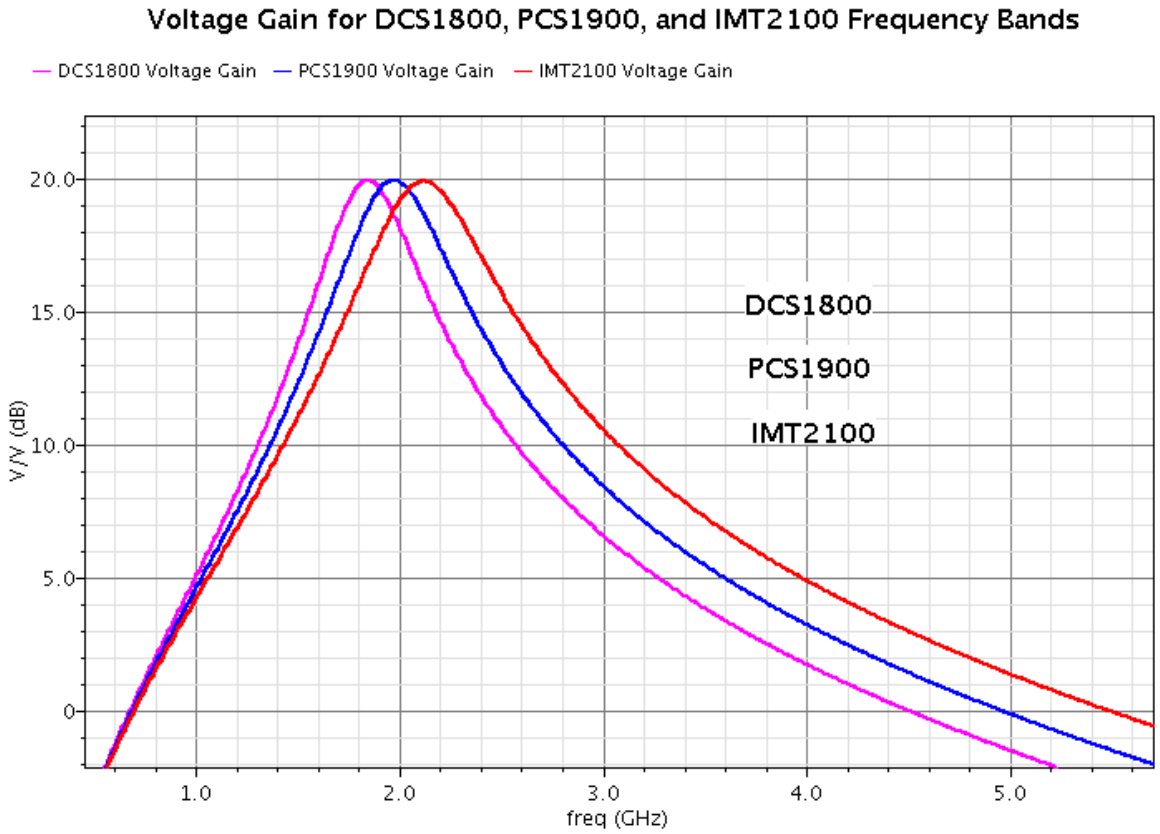

Figure 29. Conversion Gain of the proposed LNA

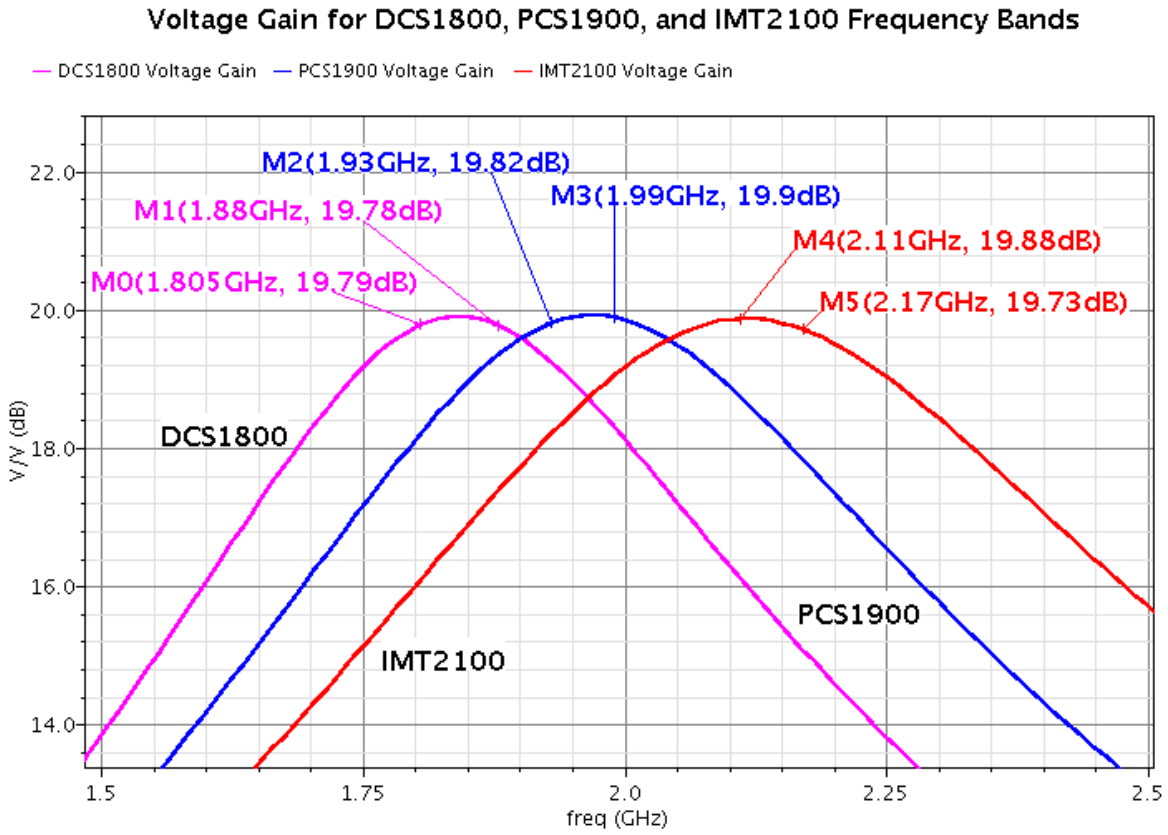

Figure 30. Conversion Gain of the proposed LNA (Close up view)

As is evident from both illustrations above, the Conversion Gain of the LNA is approximately **20dB** across all three (3) frequency bands of interest.

5.1.2 Matching

Figure 31 and Figure 32 depict the input return loss (S_{11}) of the amplifier over all three (3) wireless frequency bands.

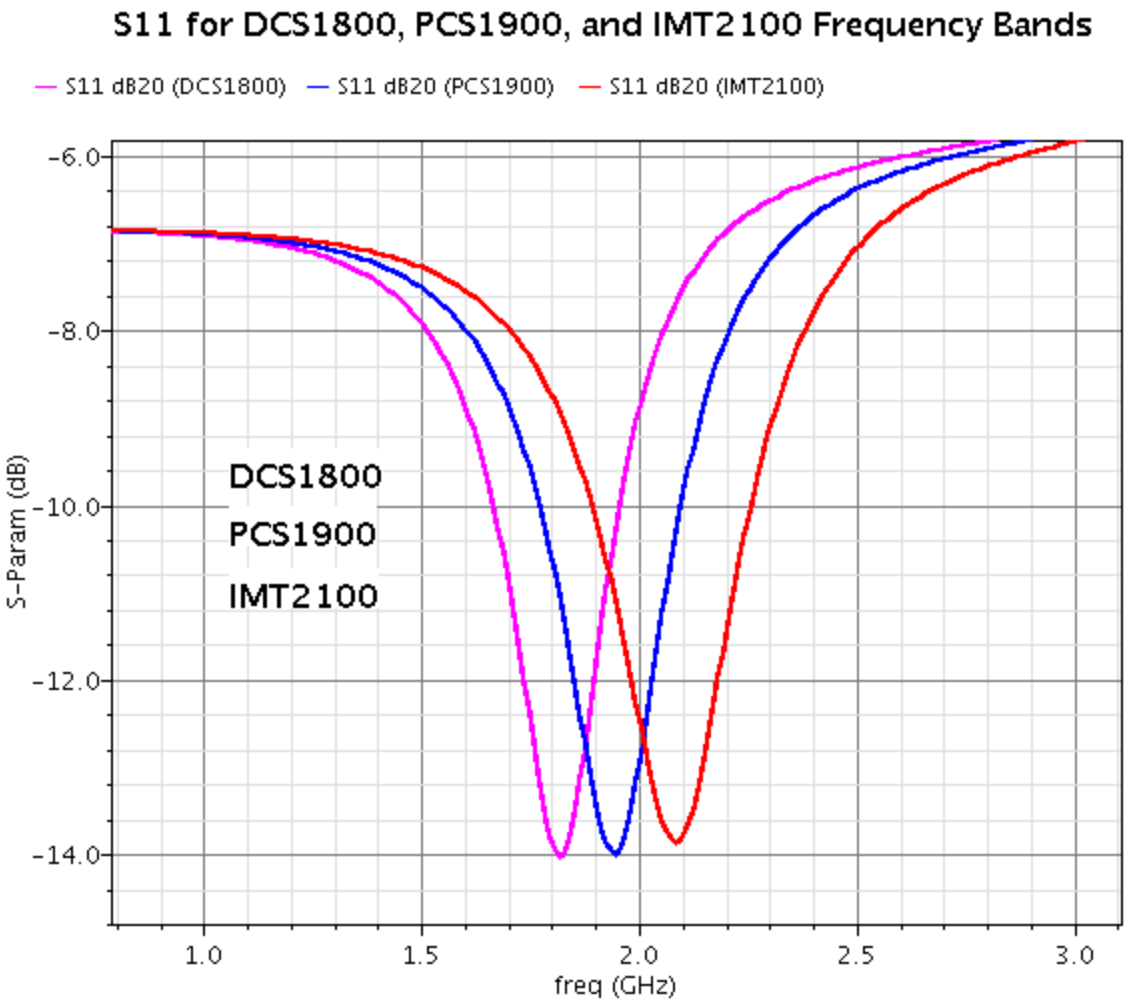

Figure 31. Input Return Loss, $\boldsymbol{S_{11}}$, of the proposed LNA

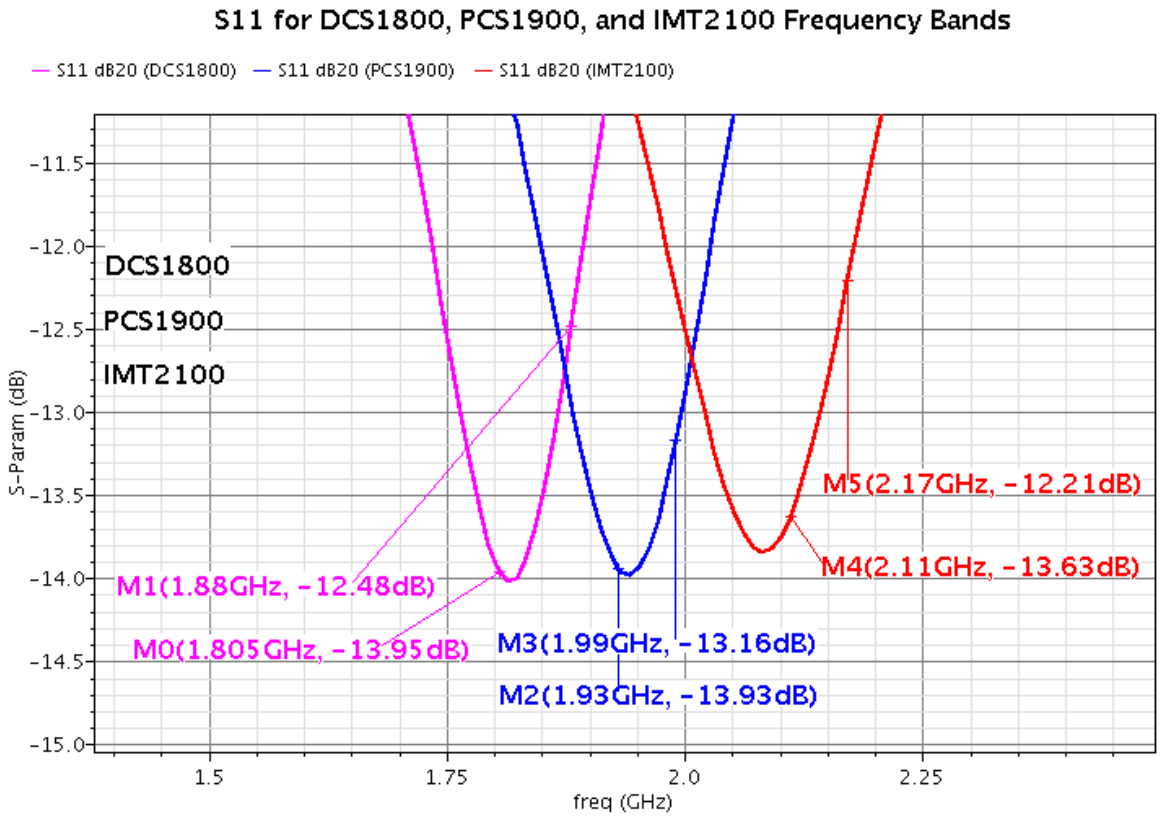

Figure 32. Input Return Loss, S_{11}, of the proposed LNA (Close up view)

Figure 32 confirms that the circuit exhibits better than **-12dB** input return loss across all three bands.

5.1.3 Isolation

Figure 33 and Figure 34 depict the isolation between the output and the input of the LNA for the three (3) frequency bands.

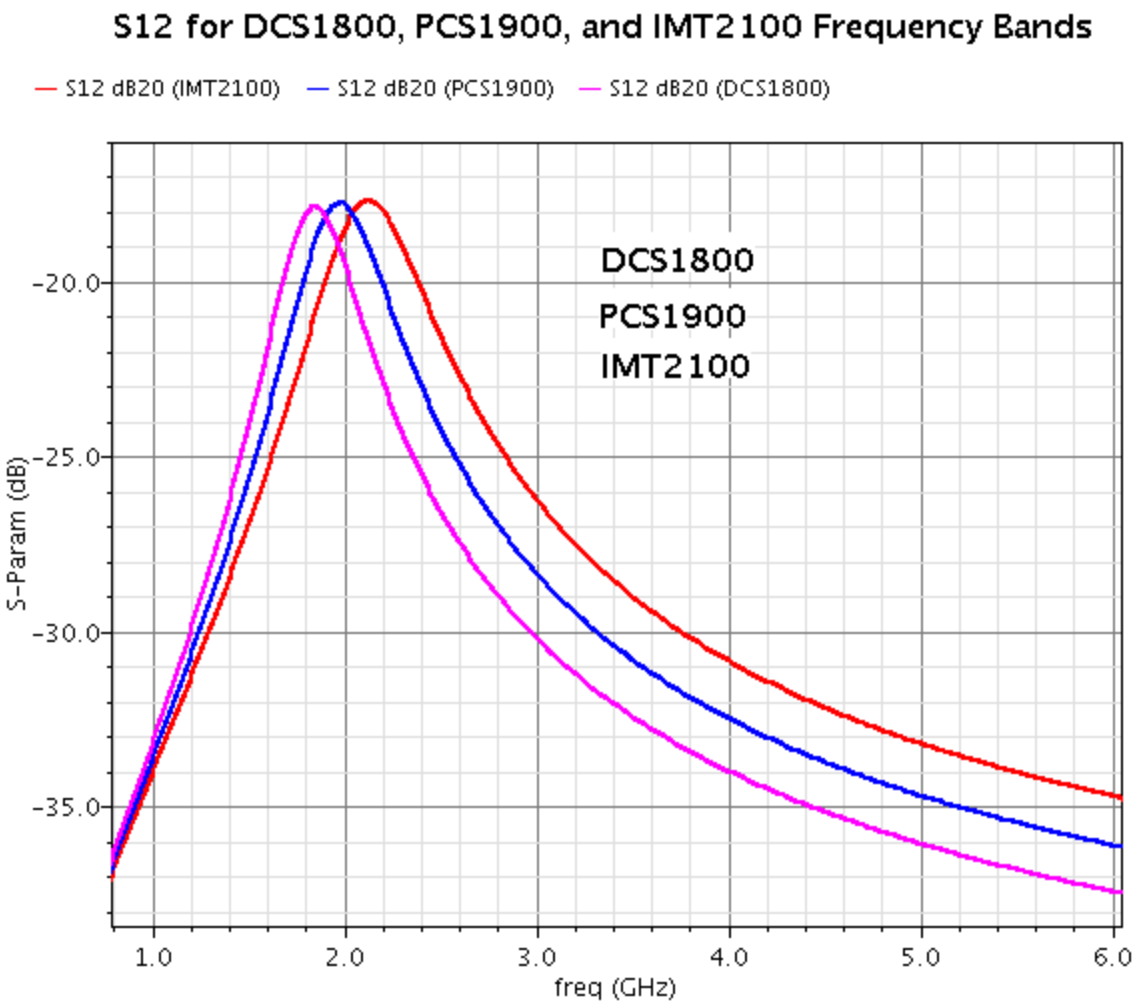

Figure 33. Output-to-Input Isolation, $\boldsymbol{S_{12}}$, of the proposed LNA

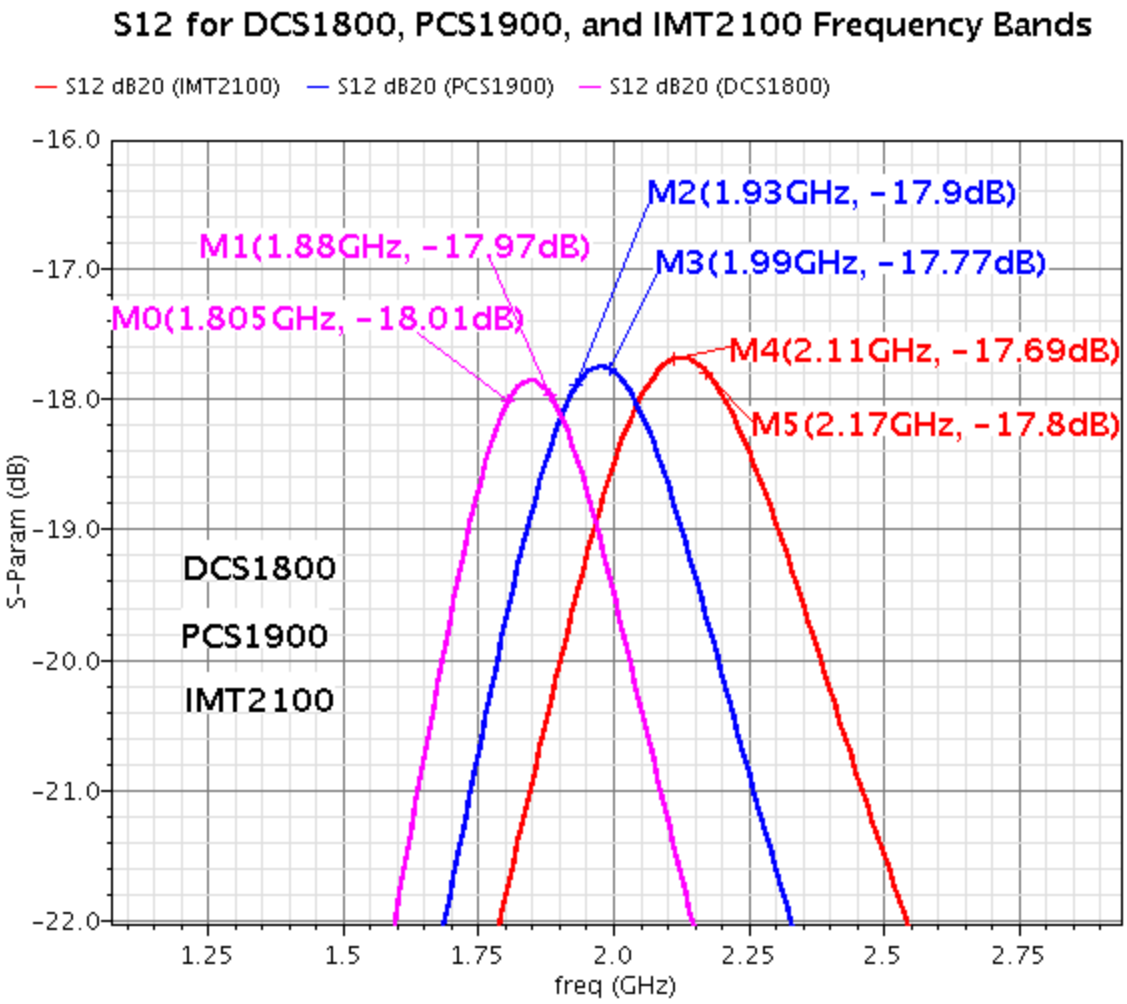

Figure 34. Output-to-Input Isolation, $\boldsymbol{S_{12}}$, of the proposed LNA (Close up view)

Figure 34 confirms that the output-to-input isolation is better than **-17.7dB** across all frequency bands of interest.

Since the proposed topology utilizes positive feedback, it is expected to observe spike (degradation) in the isolation at the resonance frequency of the tank. This is confirmed and supported by the curves in Figure 33. Nevertheless, the isolation is acceptable; as no signal will be injected to the output and that the next stage of the Frontend Receiver; i.e., Mixer, shall and will be designed to provide acceptable input return loss to compensate for the lower-than-usual, but adequate, isolation at the resonance frequencies of the tank.

Another note worth stating here is that the Output-to-Input isolation may significantly be improved by adopting a Cascode configuration as employed in [18]; however, in [18], off-chip inductors are used as current source to provide head-room for the Cascode configuration. Since elimination of the off-chip current source is one of the objectives of this work, the Cascode configuration is not feasible for our adopted circuit topology. Furthermore, the addition of another active device to the circuit, and in the signal path, will degrade the noise performance.

5.2 Noise Performance

5.2.1 Noise Figure

Figure 35 and Figure 36 demonstrate the Noise Figure curves for the three frequency bands.

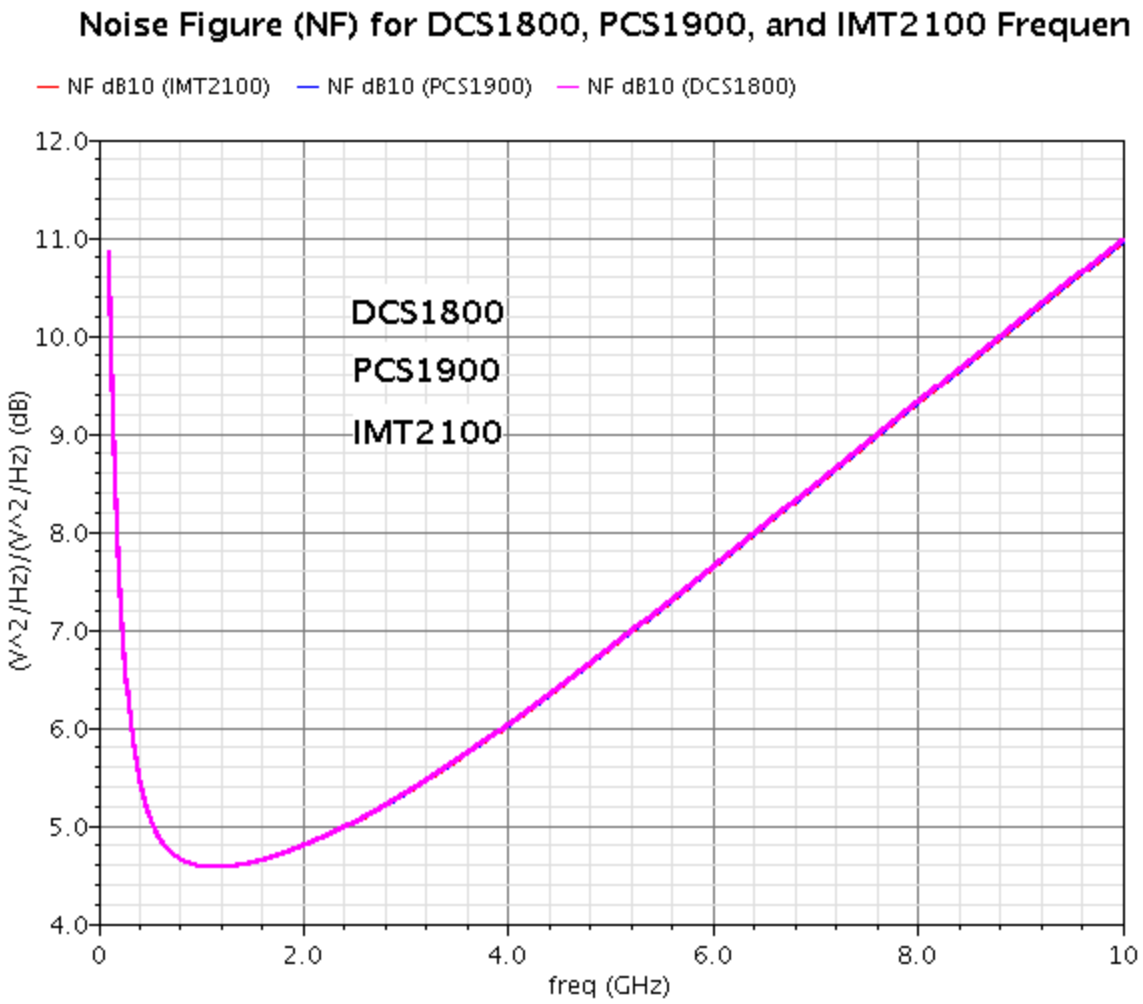

Figure 35. Noise Figure curves of the proposed LNA

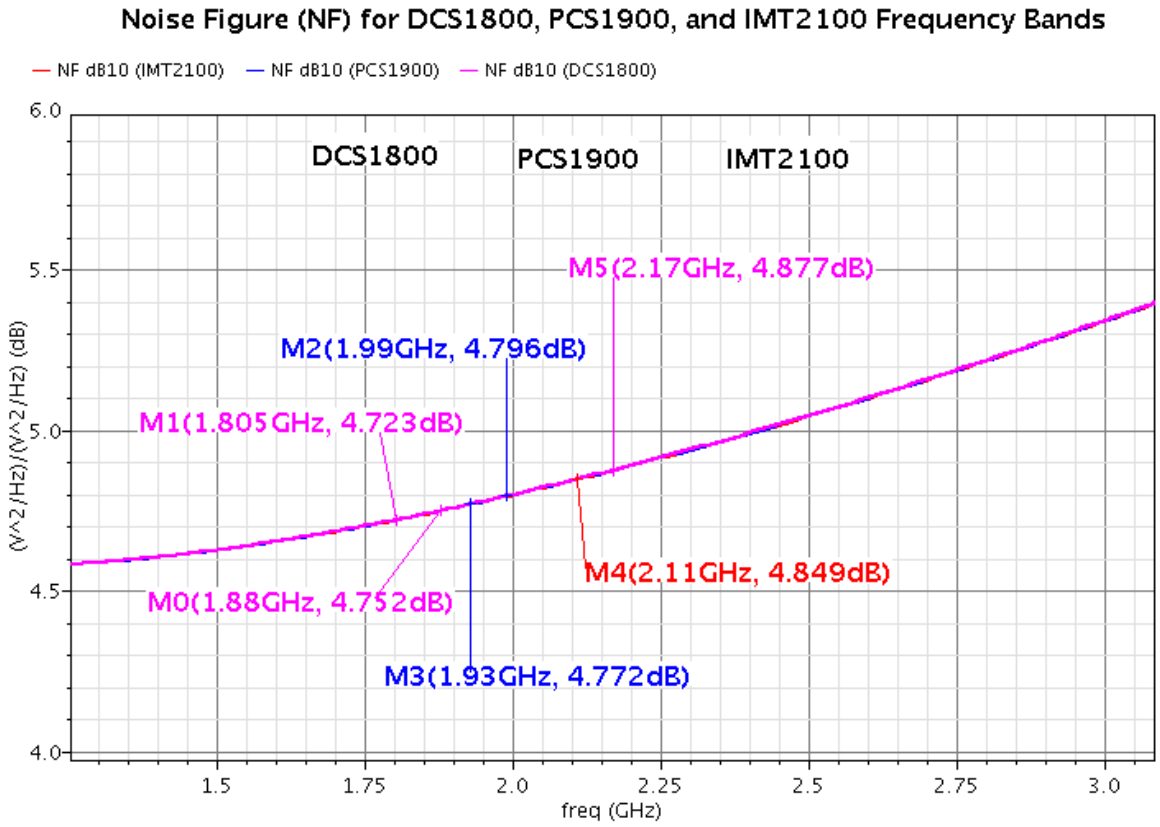

Figure 36. Noise Figure curves of the proposed LNA (Close up view)

The Noise Figure curves illustrated in Figure 36 clearly demonstrate the contribution of the Cross-Coupling Noise Cancellation Technique as discussed in Section 3.3. As will be seen in the comparison Table 7, the adopted noise cancellation technique has reduced the Noise Figure (NF) **0.5dB** and **0.7dB** for the DCS1800 and IMT2100, respectively, compared to the LNA proposed in [5].

5.2.2 Minimum Noise Figure

Figure 37 and Figure 38 depict the Minimum Noise Figure curves for the three (3) wireless bands.

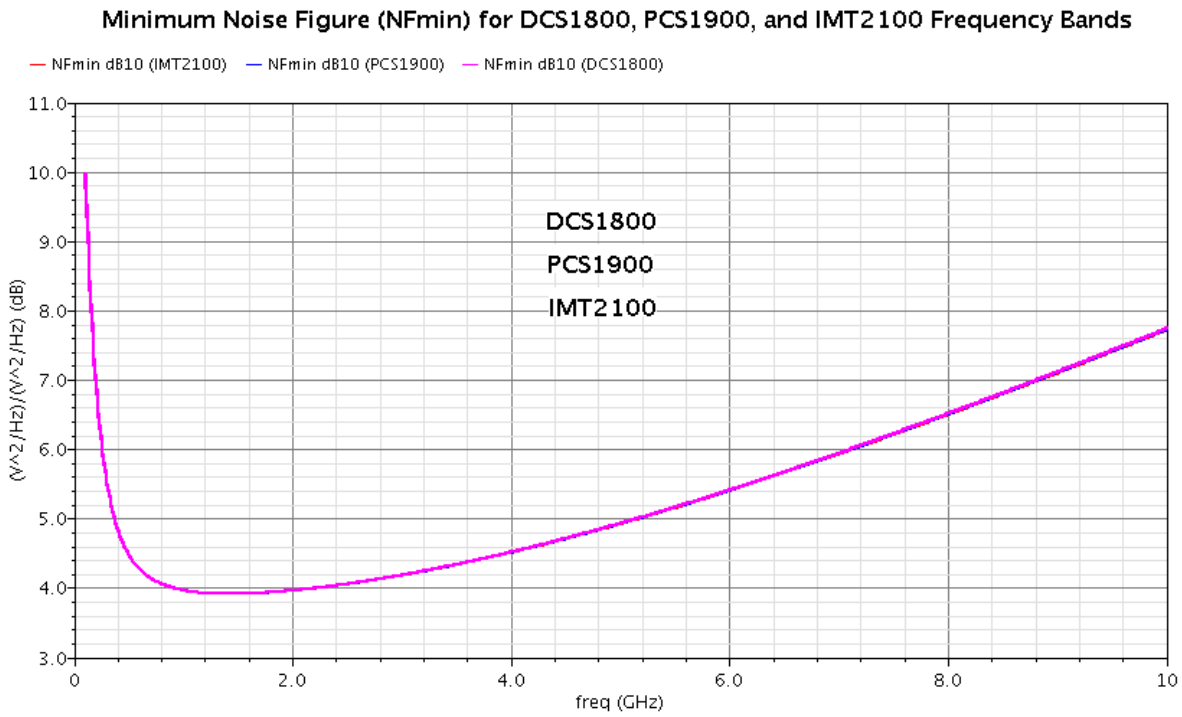

Figure 37. Minimum Noise Figure curves of the proposed LNA

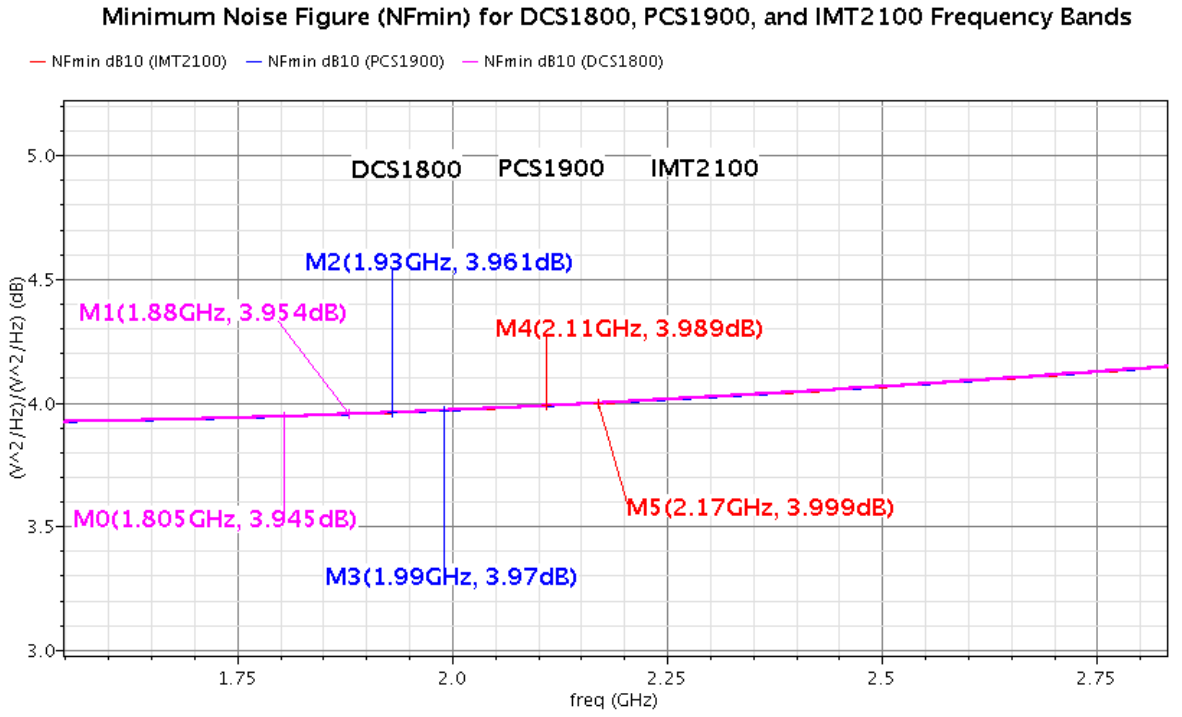

Figure 38. Minimum Noise Figure curves of the proposed LNA (Close up view)

The Minimum Noise Figure, NF_{min}, curves exhibit that the circuit Noise Figure is about **0.7dB** to **0.8 dB** higher than NF_{min} for the corresponding frequency band.

5.3 Stability Analysis

Given that the proposed LNA utilizes positive feedback, it is reasonable to verify the stability of the amplifier under varying load and source impedances. Before we proceed with presenting the source and load stability plots, it is instructive to re-examine (23). The denominator of this equation must be greater than zero (0) for the circuit to be stable; as such, we must have

(52) $$g_{m1} - g_{m3} - g_{m1}g_{m2}R_p > 0$$

Re-organizing (52), we obtain the following stability condition:

(53) $$\frac{g_{m3}}{g_{m1}} + g_{m2}R_p < 1$$

Considering the fact that g_{m3} is always significantly less than g_{m1}, and that $g_{m2}R_p$ is less than one, the condition in (52) may be fulfilled easily.

5.3.1 Load Stability Circles

Figure 39, Figure 40, and Figure 41 depict the Load Stability Circles in the Impedance Smith Chart for the DCS1800, PCS1900, and IMT2100 frequency bands, respectively. To generate these plots, the frequency was swept from 100 MHz to 10 GHz with the steps size of 50 MHz.

Since $|S_{11}| < 1$ and $|S_{22}| < 1$, for a 50Ω impedance system, the center of the normalized Smith chart falls within the stable region.

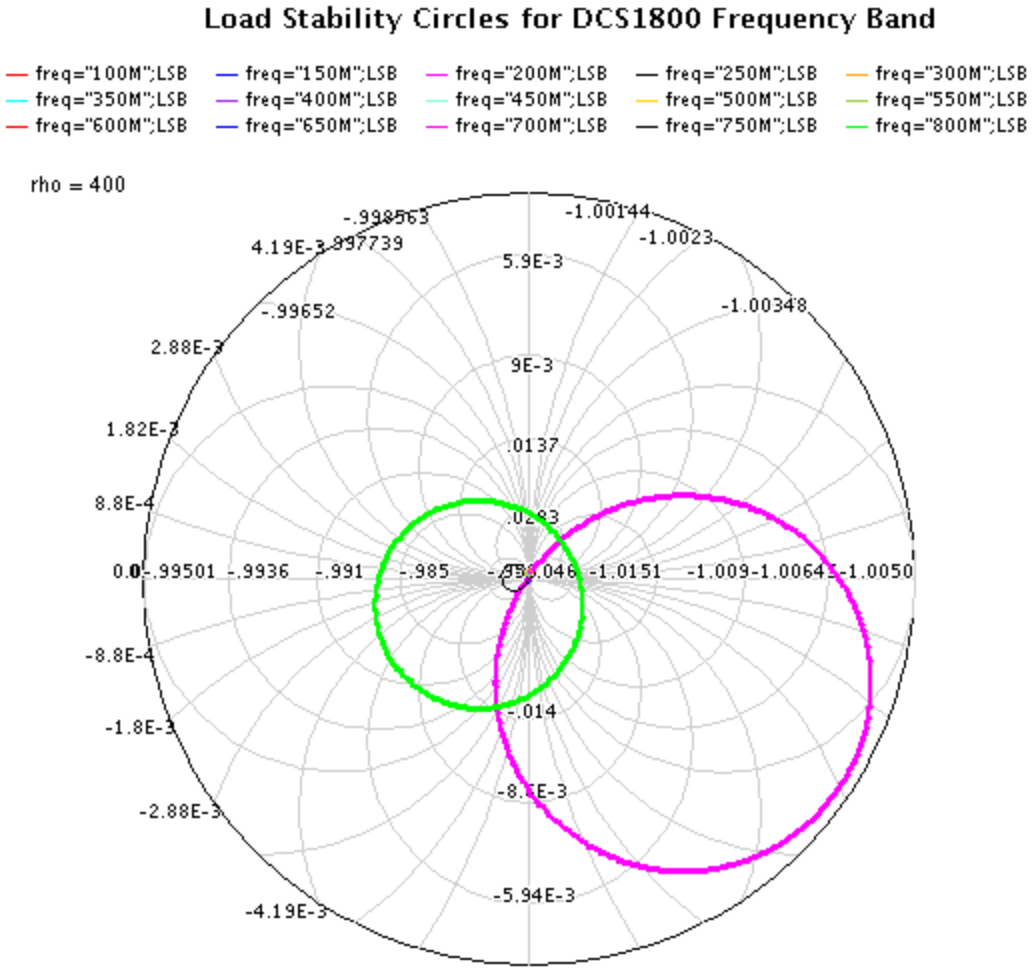

Figure 39. Load Stability circles of the proposed LNA for the DCS1800 band.

Figure 39 demonstrates that the unstable region for the load is located in a small portion of the chart (i.e., the area encompassed horizontally between points -0.99501 and -1.005 that is far from the center of the chart marked by "1" and not shown in the chart); as such, it is evident that the stable operation for the DCS1800 frequency band is guaranteed for almost every load.

It shall also be noted that the stability circles in Figure 39 are for the 1.8 GHz and 1.9 GHz frequencies, with circles for other frequencies so small to be visible.

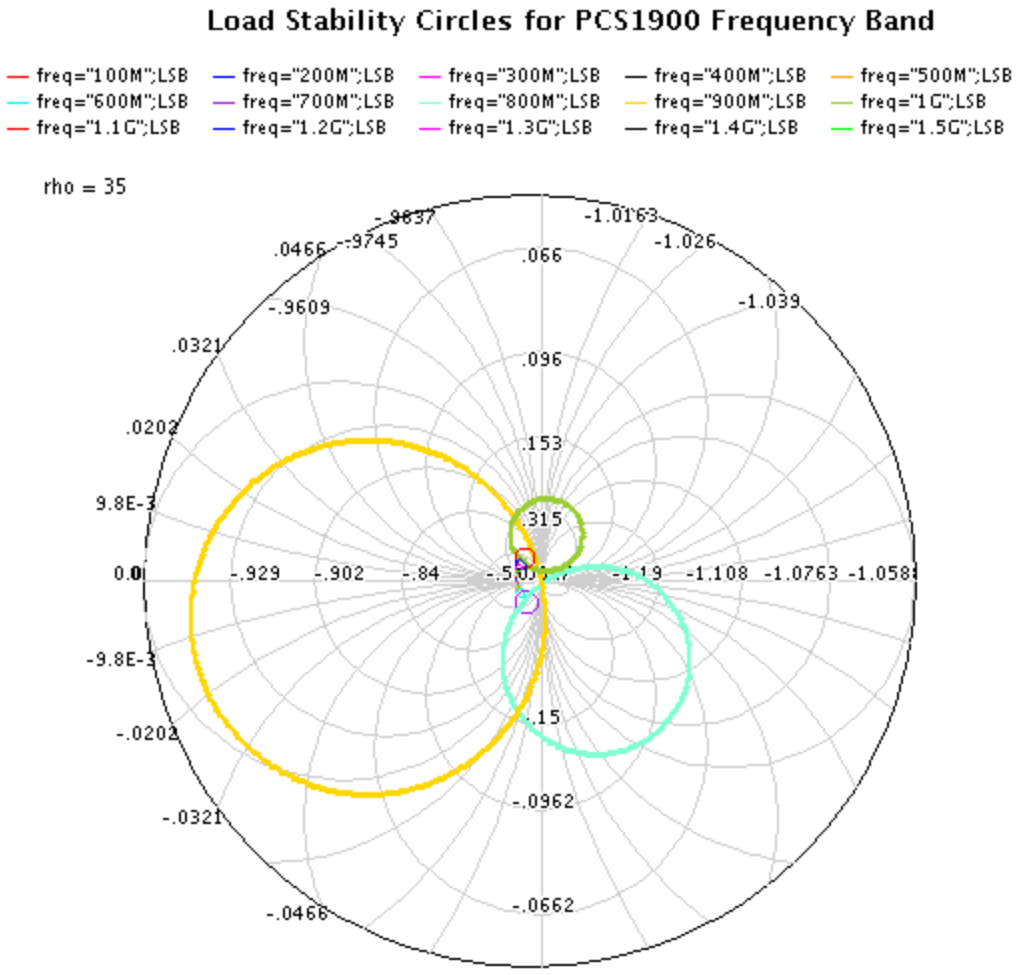

Figure 40. Load Stability circles of the proposed LNA for the PCS1900 band

Similar to the DCS1800 standard, the Load Stability circles for the PCS1900 frequency band cover a very small area on the Smith chart far away from the center marked “1” (not shown in the chart); as supported by Figure 40. As such, it is evident that the stable operation for the PCS1800 frequency band is guaranteed for almost every load.

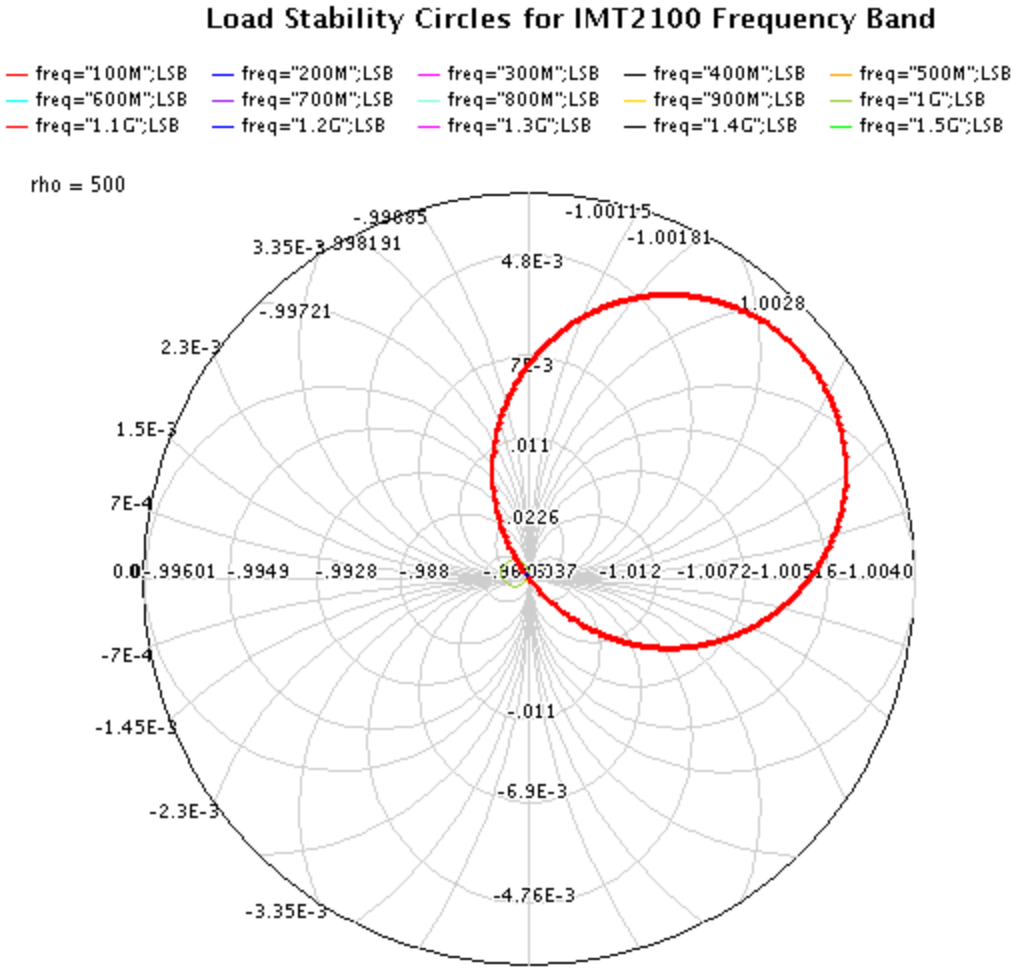

Figure 41. Load Stability circles of the proposed LNA for the IMT2100 band

Finally, and similar to the Load Stability Circles for the DCS1800 and PCS1900, Figure 41 confirms that for the IMT2100 band, the load impedances, for which the LNA is unstable, cover minute area of the Smith Chart far from the center; as such, the LNA is stable over a wide frequency band and for large span of loads.

5.3.2 Source Stability Circles

Figure 42, Figure 43, and Figure 44 depict the Source Stability Circles in the Impedance Smith Chart for the DCS1800, PCS1900, and IMT2100 frequency bands, respectively.

To generate these plots, the frequency was swept from 100 MHz to 10 GHz with the steps size of 50 MHz.

Since $|S_{11}| < 1$ and $|S_{22}| < 1$, for a 50Ω impedance system, the center of the normalized Smith chart falls within the stable region.

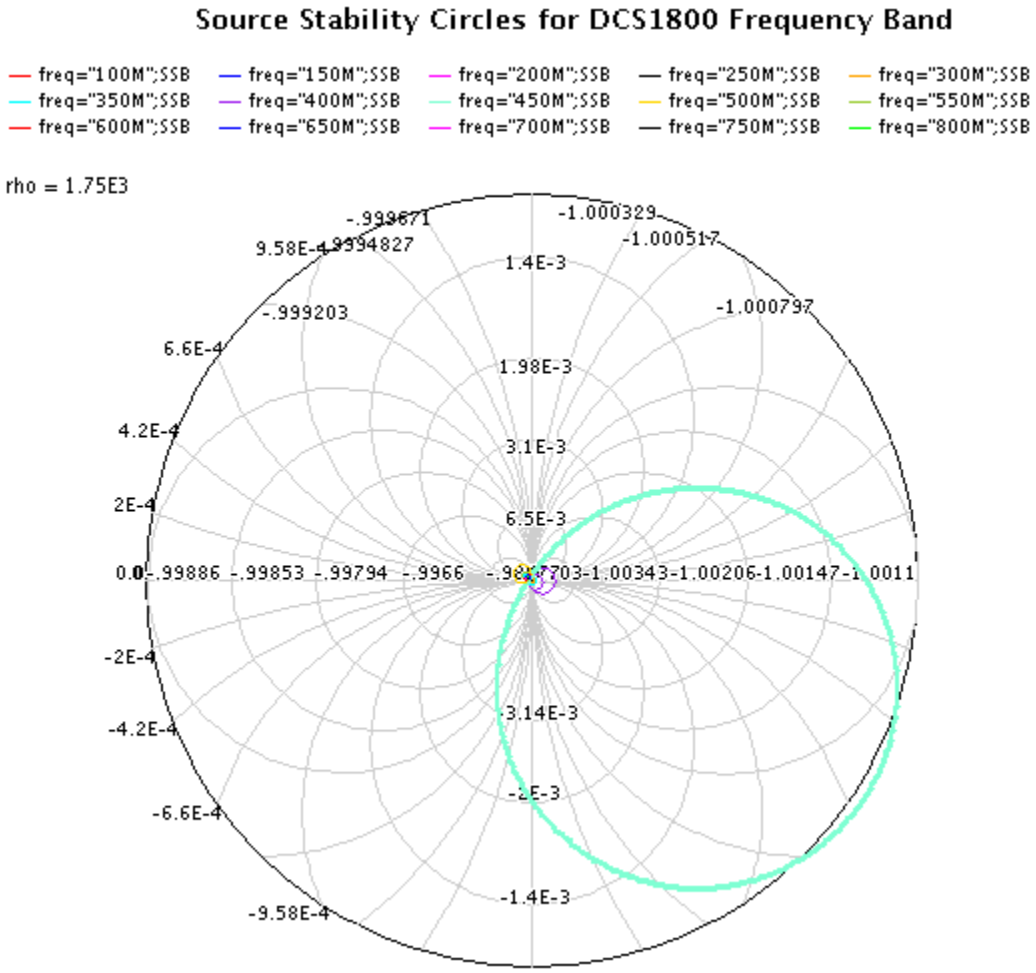

Figure 42. Source Stability circles of the proposed LNA for the DCS1800 band

Similar to the Load Stability Circles observed in Section 5.3.1, the area confined by the Source Stability circles for the DCS1800 band is both far from the center of the chart and small. Furthermore, since the Source impedance is fixed at 50Ω, it does not pose a threat to the stability

of the amplifier. As such, the LNA is stable across a wide frequency band for almost any source impedance.

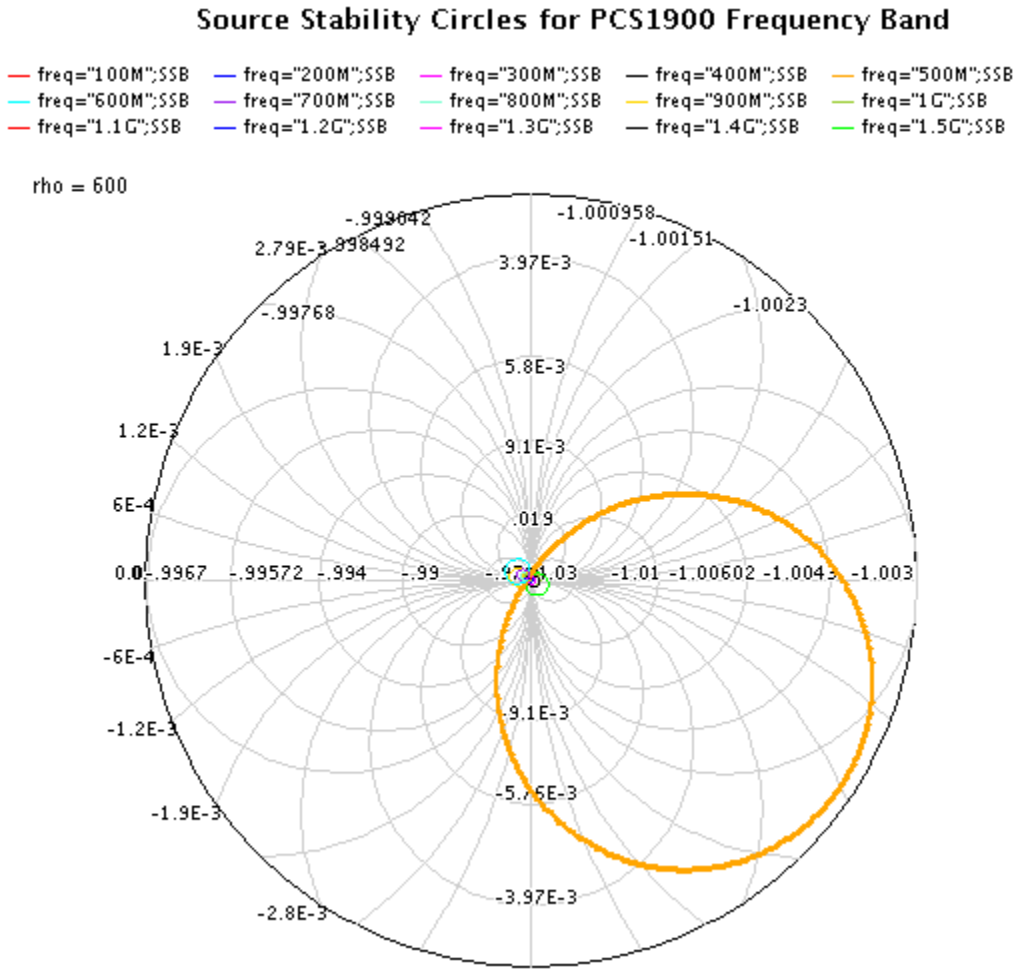

Figure 43. Source Stability circles of the proposed LNA for the PCS1900 band

Similar to the DCS1800 frequency band, Figure 43 confirms that the PCS1900 band enjoys stability for larger variation in the Source impedance and over a wide frequency band.

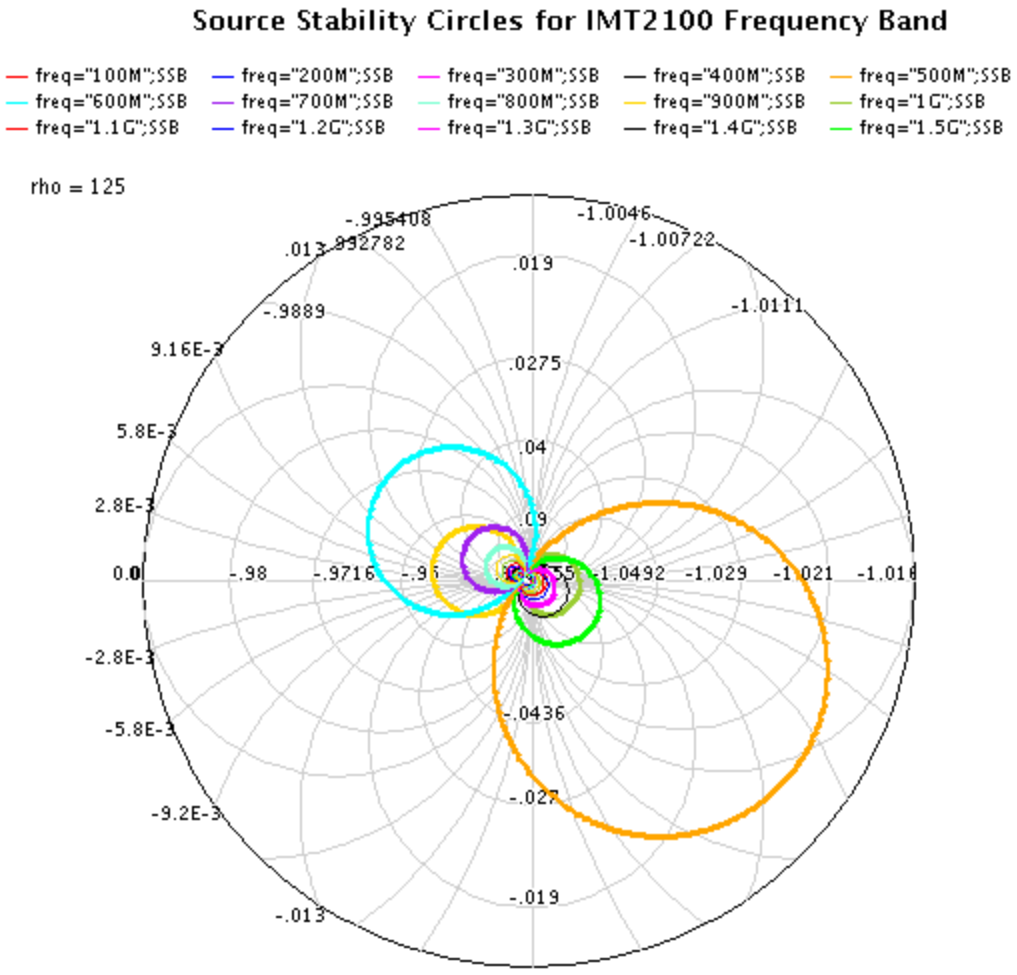

Figure 44. Source Stability circles of the proposed LNA for the IMT2100 band

Finally, the Source stability circles for the IMT2100 band cover a minute area of the Smith chart and guarantee stability under large source impedance variation and wide frequency span.

In conclusion, the LNA is stable over the frequency band of 100 MHz to 10 GHz and for almost any source and load impedance.

5.4 Linearity Analysis

In this section, we will present the simulation results for the Input-Referred 1dB Compression Point, Input-Referred Second-Order Intercept Point (IIP2), and the Input-Referred Third-Order Intercept Point (IIP3) of the proposed LNA.

5.4.1 Input-Referred 1dB Compression Point

Figure 45, Figure 46, and Figure 47 depict the simulation results for the Input-Referred 1dB Compression points for the three (3) wireless bands supported by the proposed LNA.

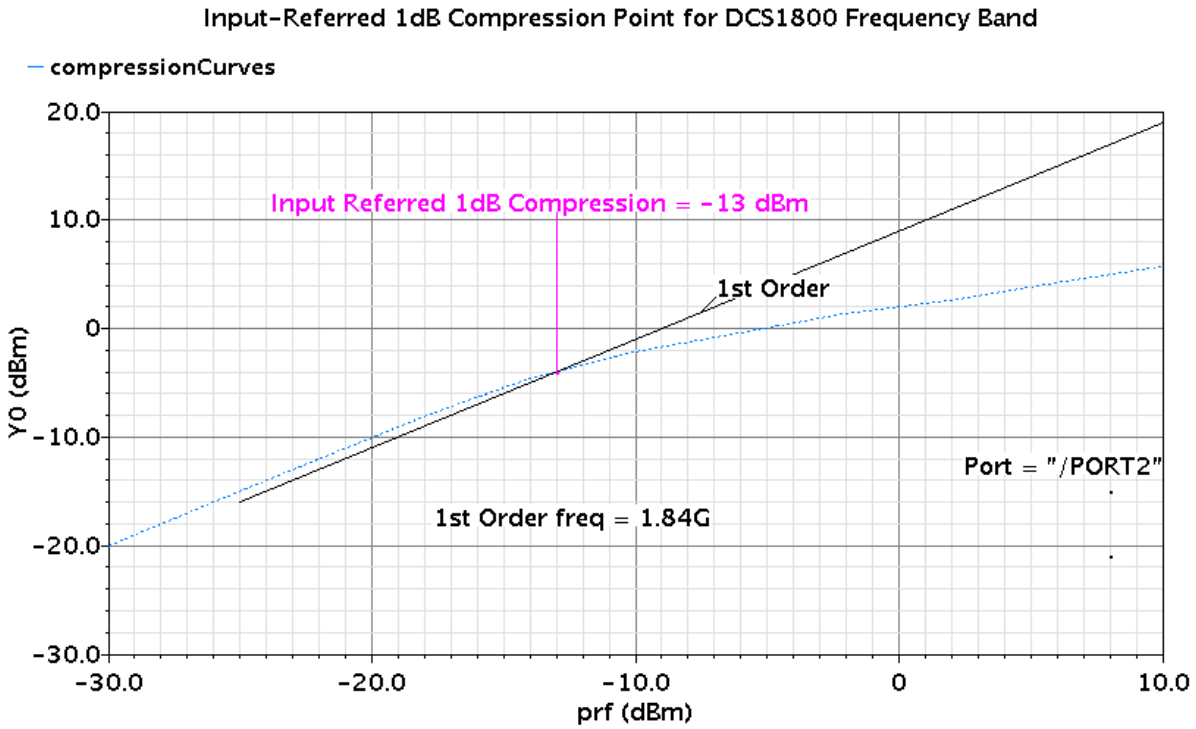

Figure 45. Input-Referred 1dB Compression Point for the DCS1800 band

Figure 45 confirms that the Input-Referred 1dB Compression Point for the DCS1800 frequency band is equal to **-13 dBm**.

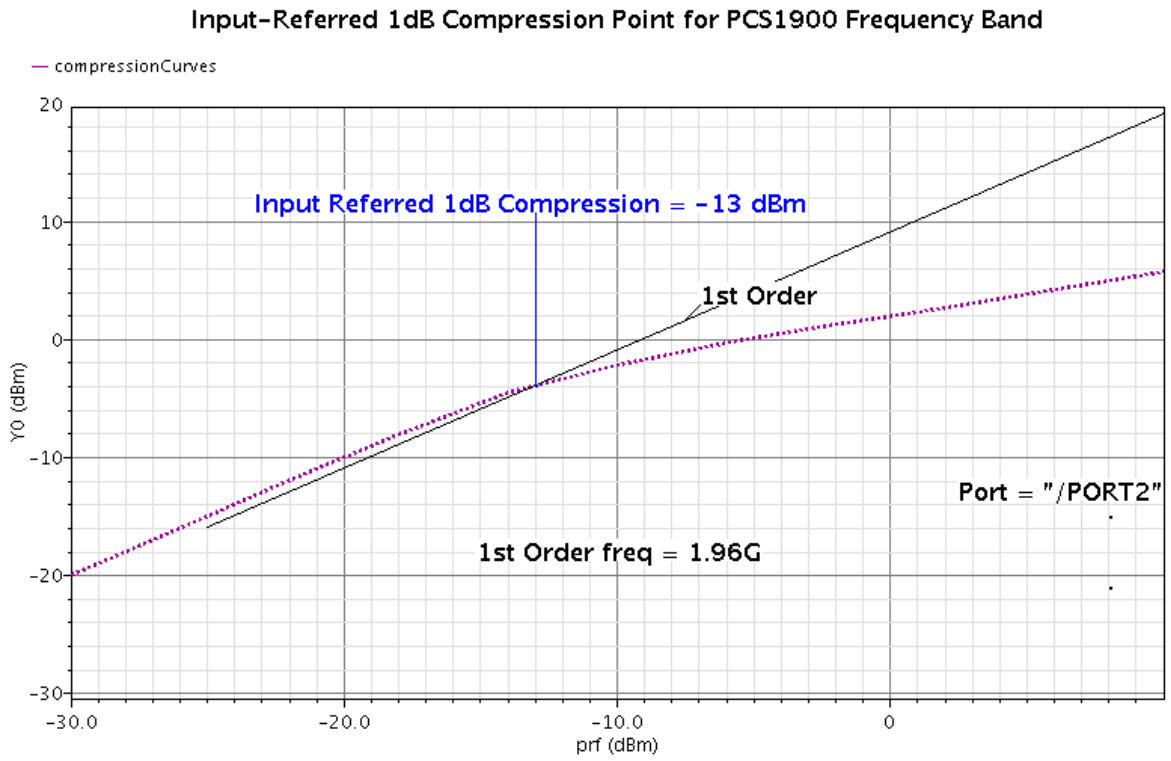

Figure 46. Input-Referred 1dB Compression Point for the PCS1900 band

Figure 46 confirms that, similar to the DCS1800 band, the Input-Referred 1dB Compression Point for the PCS1900 frequency band is equal to **-13 dBm**.

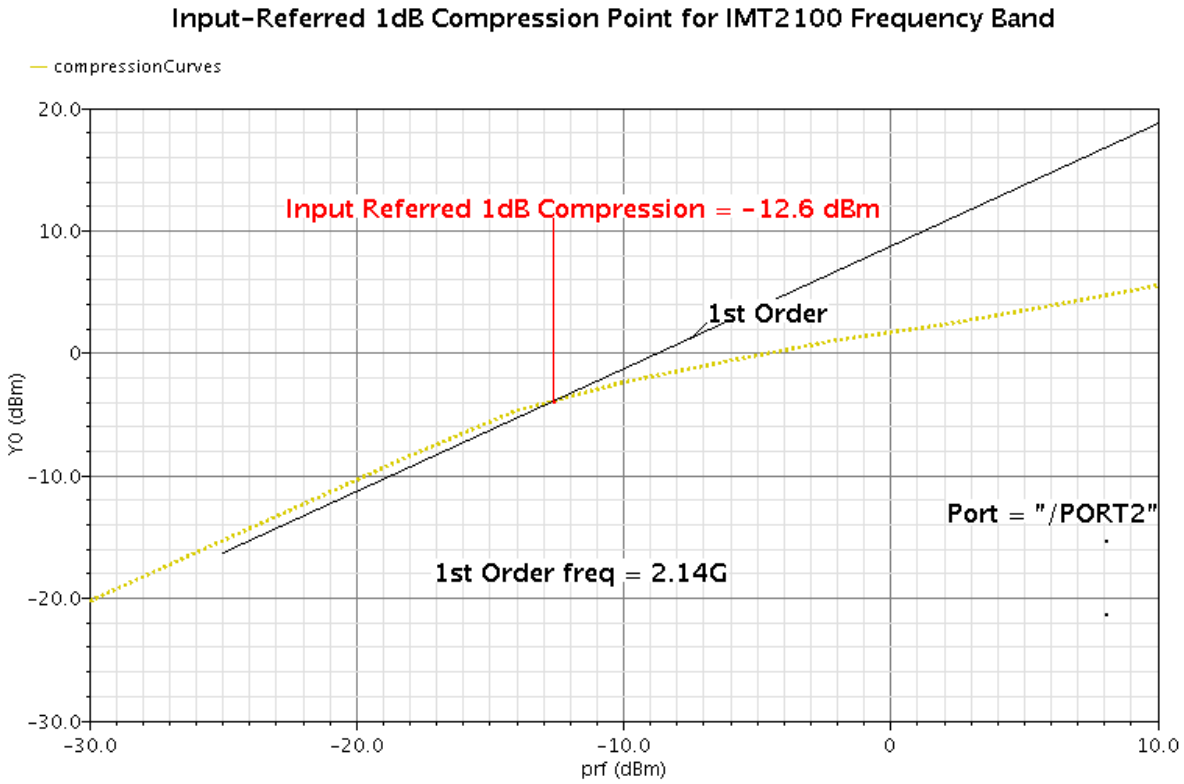

Figure 47. Input-Referred 1dB Compression Point for the IMT2100 band

Finally, Figure 47 confirms that the Input-Referred 1dB Compression Point for the IMT2100 frequency band is equal to **-12.6 dBm**.

The Input-Referred 1dB Compression Point figures for the frequency bands of interest confirm that the LNA enjoys high linearity due, in part, to the configuration adopted; i.e., Common-Gate, as well as the Feedback and the narrow-band tuned tank.

5.4.2 Input-Referred Second-Order Intercept Point (IIP2)

Figure 48, Figure 49, and Figure 50 depict the simulation results for the Input-Referred Second-Order Intercept Point (IIP2) for the three (3) wireless bands supported by the proposed LNA.

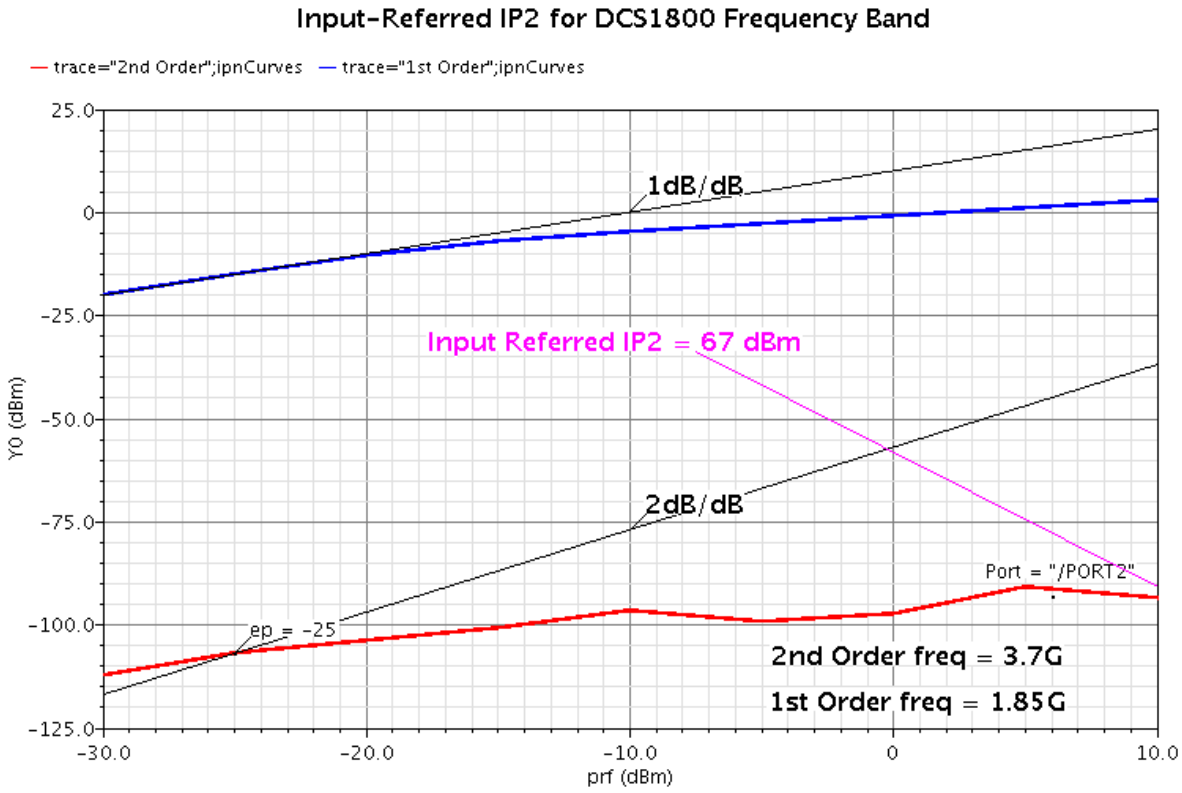

Figure 48. Input-Referred IP2 of the proposed LNA for the DCS1800 band

Figure 48 confirms that the Input-Referred IP2 for the DCS1800 frequency band is equal to **+67 dBm**. This high IIP2 is owed to the highly frequency-selective nature of the tuned tank as evident in Figure 29.

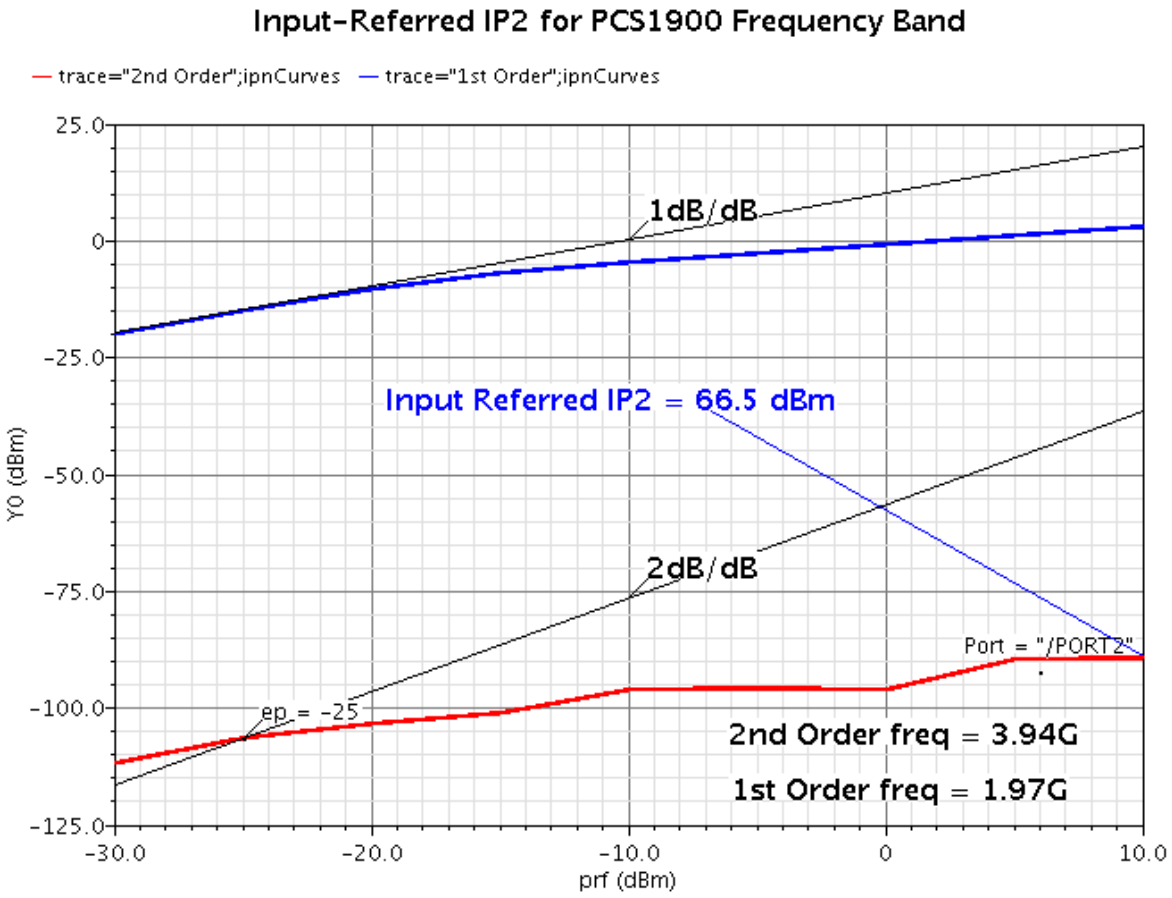

Figure 49. Input-Referred IP2 of the proposed LNA for the PCS1900 band

Similar to the DCS1800 frequency band, Figure 49 confirms that the Input-Referred IP2 for the PCS1900 frequency band is high and equal to **+66.5 dBm** due to the same characteristics of the LNA as mentioned above.

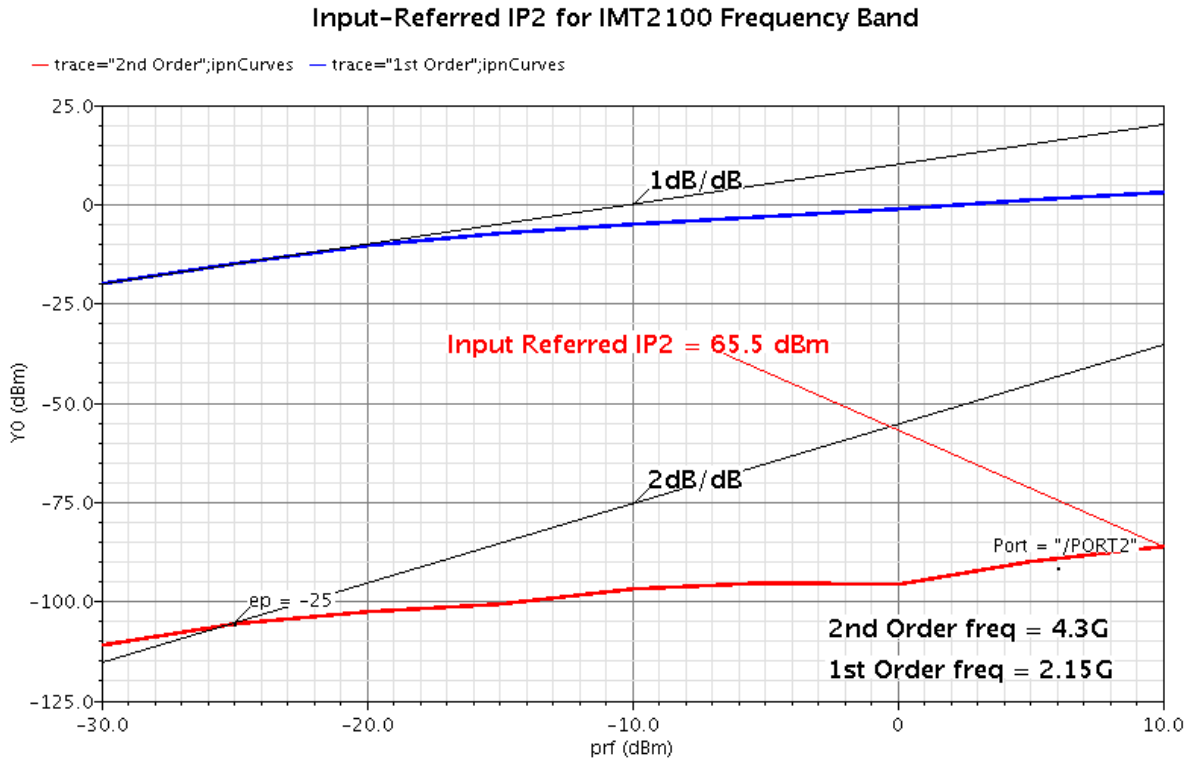

Figure 50. Input-Referred IP2 of the proposed LNA for the IMT2100 band

Finally, and similar to the other frequency bands, Figure 50 confirms that the Input-Referred IP2 for the IMT2100 frequency band is equal to **+65.5 dBm**.

5.4.3 Input-Referred Third-Order Intercept Point (IIP3)

Figure 51, Figure 52, and Figure 53 depict the simulation results for the Input-Referred IP3 for the three (3) wireless bands supported by the proposed LNA.

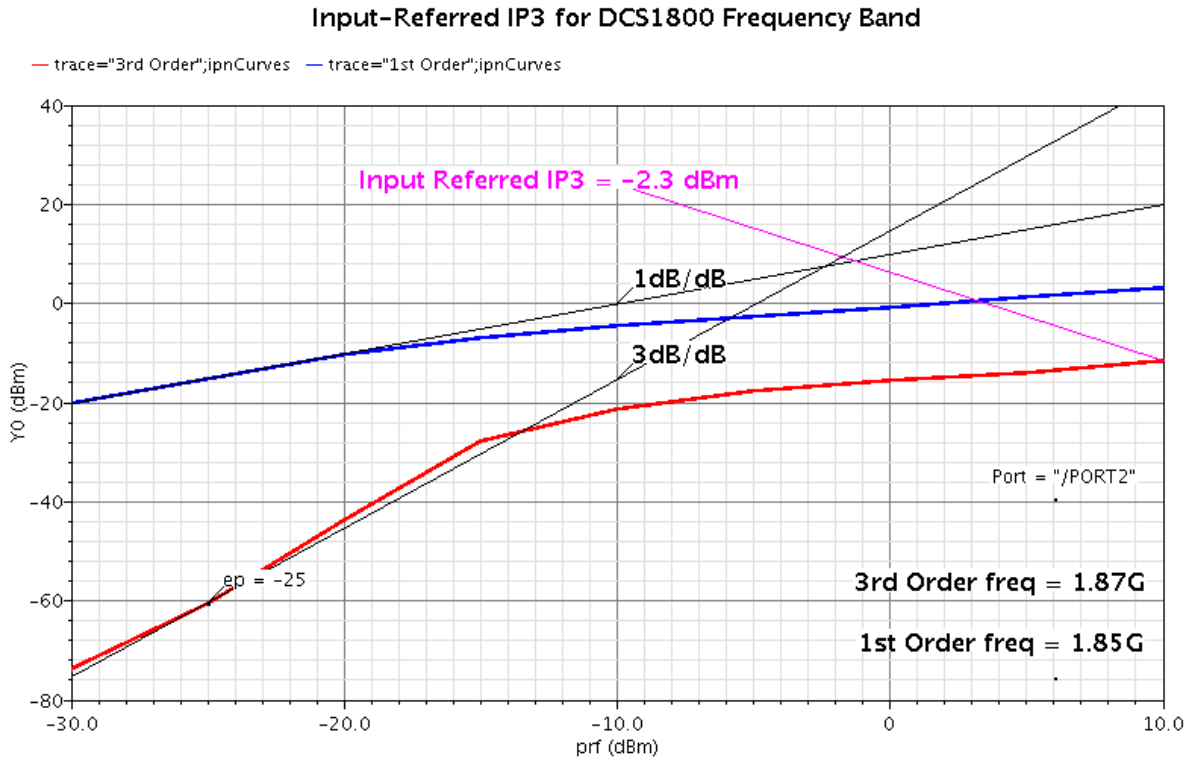

Figure 51. Input-Referred IP3 of the proposed LNA for the DCS1800 band

Figure 51 confirms that the Input-Referred IP3 for the DCS1800 frequency band is equal to **-2.3 dBm**. This significant IIP3 is achieved due to the adoption of the Common-Gate topology and maintaining the Loop Gain of the Feedback network as small as possible [5]. This is evident from the small transconductance value of the feedback transistor as listed in Table 5.

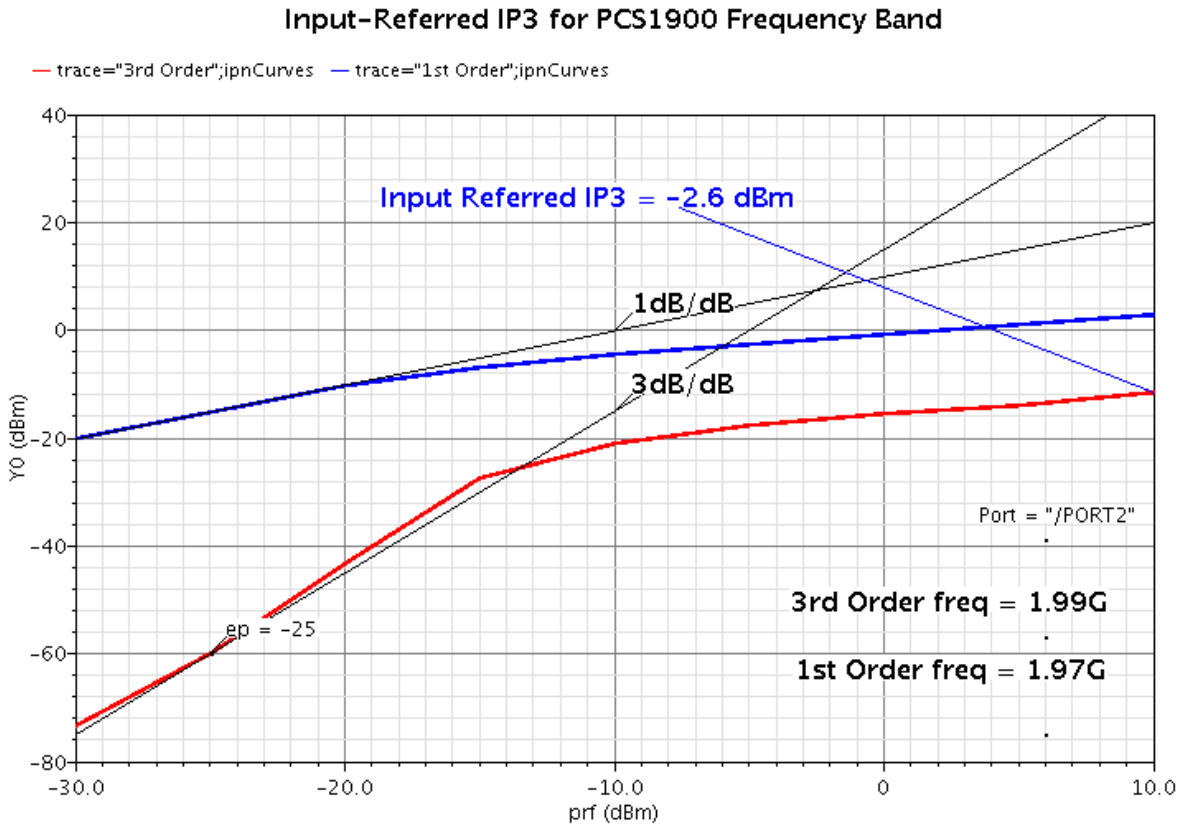

Figure 52. Input-Referred IP3 of the proposed LNA for the PCS1900 band

Figure 52 confirms that the Input-Referred IP3 for the PCS1900 frequency band is equal to **-2.6 dBm**.

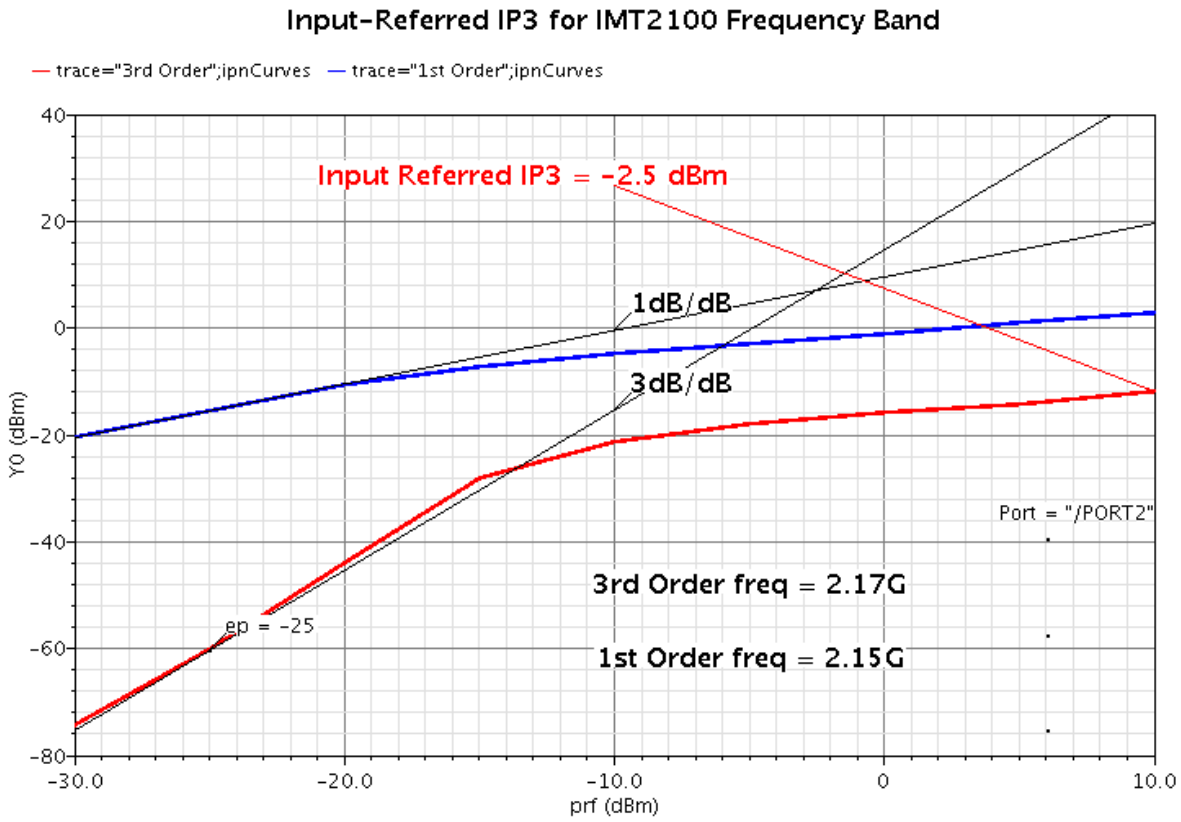

Figure 53. Input-Referred IP3 of the proposed LNA for the IMT2100 band

Figure 53 confirms that the Input-Referred IP3 for the IMT2100 frequency band is equal to **-2.5 dBm**.

5.5 LNA Performance Summary

Table 6 summarizes the performance characteristics of the proposed LNA.

Parameter	DCS1800	PCS1900	AWS1700 & IMT2100
Conversion Gain (dB)	**19.8**	**19.8**	**19.7**
S_{11} (dB)	**< -12.5**	**< -13.2**	**< -12.2**
S_{12} (dB)	**< -17.8**	**< -17.7**	**< -17.7**
Noise Figure (dB)	**< 4.8**	**< 4.8**	**< 4.9**
Input-Ref. 1dB CP (dBm)	**-13**	**-13**	**-12.6**
Input-Referred IP2 (dBm)	**+67**	**+66.5**	**+65.5**
Input-Referred IP3 (dBm)	**-2.3**	**-2.6**	**-2.5**
Supply Voltage (V)	**1.2**		
Power Consumption (mW)	**10.8**		
Technology	**0.12 µm CMOS**		

Table 6. Performance Characteristics of the Proposed LNA

We are now at a position to compare the performance of the proposed LNA with that reported in [5].

5.6 Performance Comparison

Table 7 provides the comparison of the performance characteristics of the proposed LNA with those reported in [5].

Parameter	This Work			As reported by [5]		
	DCS1800	PCS1900	AWS1700 & IMT2100	DCS1800	IMT2100	802.11 b-g
Conversion Gain (dB)	19.8	19.8	19.7	13.5 - 28.5	14.5 – 29.5	8.4 – 23.4
S_{11} (dB)	< -12.5	< -13.2	< -12.2	-32	-20	-20
S_{12} (dB)	< -17.8	< -17.7	< -17.7	N/A	N/A	N/A
Noise Figure (dB)	< 4.8	< 4.8	< 4.9	5.2	5.6	5.8
Input-Ref. 1dB CP (dBm)	-13	-13	-12.6	N/A	N/A	N/A
Input-Referred IP2 (dBm)	+67	+66.5	+65.5	50	51	54
Input-Referred IP3 (dBm)	-2.3	-2.6	-2.5	-7.5	0	-4.8
Supply Voltage (V)	1.2			1.5		
Power Consumption (mW)	10.8			20/24		
Technology	0.12 µm CMOS			0.13 µm CMOS		

Table 7. Comparison of the Performance Characteristics with [5]

Table 7 demonstrates that the proposed LNA, in addition to utilizing on-chip current source and only one inductor for all three bands of interest, is superior to that proposed in [5] in the following areas: Noise Figure, IIP2, IIP3, Supply Voltage, Power Consumption, and the feature size of the CMOS technology.

These advantages of the proposed LNA make it a good candidate for utilization in the Frontend of a Reconfigurable Receiver for the Cellular Frequency Bands.

6 Conclusion and Future Work

6.1 Conclusion

This document presented the review and analysis of the state-of-the-art Receiver Frontend Architectures for wireless communications, and identified the most appropriate topology for Reconfigurable Multi-Standard applications.

Furthermore, the topology of a multi-band and reconfigurable LNA was introduced and its performance was analyzed theoretically and verified by simulation. The proposed LNA topology utilizes positive feedback for increasing gain and providing flexibility in matching, cross-coupling configuration for noise cancellation, and on-chip current source. The LNA supports the three major mobile wireless bands; i.e., DCS1800 (primarily in Europe and Asia), PCS1900 (mostly in the Americas), AWS1700 (in North America), and IMT2100 (the rest of the world) for global roaming.

6.2 Future Work

There are several areas of research and simulation work that could follow the current effort.

One such area is the implementation of the Passive Mixer in order to verify the performance of the combined LNA and Mixer against the pertinent regulatory standards and provide a fair comparison with the performance reported in other publications; especially in the areas of IIP2 and IIP3, which are heavily affected by the second stage characteristics.

Furthermore, the IIP3 and the Output-to-Input isolation are areas of importance that require further attention and improvement. IIP3 may be improved by increasing the Overdrive Voltage [5]. However, with on-chip current source and supply voltage of only 1.2V, it is challenging, if not impossible. Furthermore, the Output-to-Input isolation improvement may be

achieved by adopting Cascode configuration; however, with on-chip current source and the 1.2V supply voltage, it is extremely difficult. As such, a higher-voltage power supply architecture will be investigated; potentially using start-up circuits to prevent the circuit elements from exposure to higher-than-recommended voltage levels and not affect device reliability.

It is also warranted to investigate techniques to improve the noise figure of the proposed LNA to levels near or below 3dB. The topology in [18] achieves lower noise figure primarily because of utilizing positive and negative feedback networks concurrently as well as off-chip inductors that is in contrast to the objective of this work. Had the [18] used on-chip current source in place of off-chip inductors, its reported Noise Figure would have been higher, as no noise cancellation technique is employed.

References

[1] CDMA Development Group. www.cdg.org.

[2] GSM Association. www.gsmworld.com.

[3] S. Lou and H. C. Luong, "A 0.8GHz–10.6GHz SDR Low-Noise Amplifier in 0.13-µm CMOS" *IEEE 2008 Custom Integrated Circuits Conference (CICC).*

[4] P. Rossi, A. Liscidini, M. Brandolini, and F. Svelto, "A variable gain RF front-end, based on a voltage-voltage feedback LNA, for multistandard applications," *IEEE J. Solid-State Circuits*, vol. 40, no. 3, pp. 690–697, Mar. 2005.

[5] A. Liscidini, M. Brandolini, D. Sanzogni, and R. Castello, "A 0.13µm CMOS front-end for DCS1800/UMTS/802.11b-g with multi-band positive feedback low noise amplifier," *IEEE J. Solid-State Circuits*, vol. 41, no. 4, pp. 981–989, Apr. 2006.

[6] A. Amer, E. Hegazi, and H. F. Ragaie, "A 90-nm Wideband Merged CMOS LNA and Mixer Exploiting Noise Cancellation," *IEEE J. Solid-State Circuits*, vol. 42, no. 2, pp. 323–328, Feb. 2007.

[7] H. Hashemi and A. Hajimiri, "Concurrent Multiband Low-Noise Amplifiers—Theory, Design, and Applications," *IEEE Transactions on Microwave Theory and Techniques*, vol. 50, no. 1, pp. 288-301, Jan. 2002.

[8] D. K. Shaeffer and T. H. Lee, "A 1.5-V, 1.5-GHz CMOS low noise amplifier," *IEEE J. Solid-State Circuits*, vol. 32, no. 5, pp. 745–759, May 1997.

[9] A. Liscidini, M. Brandolini, P. Rossi, F. Torrisi, and F. Svelto, "Design methodology of feedback-LNAs for GHz applications," in *Proc. Bipolar/BiCMOS Circuits and Technology Meeting (BCTM)*, Sep. 13–14, 2004, pp. 253–256.

[10] B. Razavi, *Design of Analog CMOS Integrated Circuits*, New York: McGraw-Hill, 2001.

[11] F. Bruccoleri, E. A. M. Klumperink, and B. Nauta, "Wide-band CMOS low-noise amplifier exploiting thermal noise canceling," *IEEE J. Solid-State Circuits*, vol. 39, no. 2, pp. 275–282, Feb. 2003.

[12] Adiseno, M. Ismail, and H. Olsson, "A wide-band RF front-end for multiband multistandard high-linearity low-IF wireless receivers," *IEEE J. Solid-State Circuits*, vol. 37, no. 9, pp. 1162–1168, Sep. 2002.

[13] P. Rossi, A. Liscidini, M. Brandolini, and F. Svelto, "A 2.5 dB NF direct conversion receiver front-end for HiperLAN2/IEEE802.11a," in *IEEE Int. Solid-State Circuits Conf. (ISSCC) Dig. Tech. Papers*, vol. 1, Feb. 2004, pp. 102–103.

[14] D. J. Allstot, X. Li, and S. Shekhar, "Design considerations for CMOS low-noise amplifiers," in *Proc. IEEE Radio Frequency Integrated Circuits (RFIC) Symp*., Jun. 2004, pp. 97–100.

[15] D. Cassan, J. Long, "A 1V Transformer Feedback Low-Noise Amplifier for 5GHz Wireless LAN in 0.18μm CMOS," *IEEE J. Solid-State Circuits*, vol. 38, pp. 427-435, Mar. 2003.

[16] W. Zhuo, S. Embabi, J. P. de Gyvez, and E. Sanchez-Sinencio, "Using capacitive cross-coupling technique in RF low noise amplifiers and down-conversion mixer design," *European Solid-State Circuits Conf.*, pp. 77-80, Sep. 2000.

[17] T. Cho et al, "A Single-Chip CMOS Direct-Conversion Transceiver for 900MHz Spread-Spectrum Digital Cordless Phones," *ISSCC Digest of Technical Papers*, Feb 1999, pp. 228-229.

[18] A. Liscidini et al., "Analysis and Design of Configurable LNAs in Feedback Common-Gate Topologies," *IEEE Transactions on Circuits and Systems—II: Express Briefs*, vol. 55, no. 8, August 2008.

[19] M. Brandolini et al., "Reconfigurable Si RF Receiver Front-Ends for Multi-Standard Radios," *Proceedings of the 1st European Wireless Technology Conference*, October 2008, pp. 33-36.

[20] M. Brandolini, et al., "Towards Multi-Standard Mobile Terminals: Fully Integrated Receivers Requirements and Architectures," *IEEE Transactions on Microwave Theory and Techniques*, February 2005.

[21] *Digital Cellular Telecommunications System (Phase 2); Radio Transmission and Reception*, GSM Standard 05 05, 1999.

[22] J. Ryynanen, et al., "A Single-Chip Multimode Receiver for GSM900, DCS1800, PCS1900, and WCDMA", *IEEE Journal of Solid State Circuits*, vol.38, n.4, pp.594-602, April 2003.

[23] M. Brandolini, et al., "A +78 dBm IIP2 CMOS Direct Downconversion Mixer for Fully Integrated UMTS Receivers," *IEEE J. Solid-State Circuits*, vol. 41, no. 3, pp. 552-559, March 2006.

[24] H. Darabi, et al., "Analysis and Optimization of Current-Driven Passive Mixers in Narrowband Direct-Conversion Receivers," *IEEE J. Solid-State Circuits*, vol. 44, no. 10, pp. 2678-2688, October 2009.

[25] P. Cruz, et al., "Designing and Testing Software-Defined Radios," *IEEE Microwave Magazine*, pp. 83-94, June 2010.

[26] D. Manstretta, et al., "Second-order inter-modulation mechanisms in CMOS downconverters," *IEEE J. Solid-State Circuits*, vol. 38, no. 3, pp. 394–406, Mar. 2003.

[27] M. Brandolini, et al., "A 0.18 μm CMOS direct down-converter for highly integrated 3G receivers," *Analog Integrated Circuit Signal Processing*, pp. 35-42, 2007.

[28] J. Borremans, et al., "A 40nm CMOS Highly Linear 0.4-to-6GHz Receiver Resilient to 0dBm Out-of-Band Blockers," in *IEEE Int. Solid-State Circuits Conf. (ISSCC) Dig. Tech. Papers*, Session 3, Feb. 2011, pp. 62–64.

[29] M. C. M. Soer, et al., "A 0.2-to-2.0GHz 65nm CMOS Receiver Without LNA Achieving >11dBm IIP3 and <6.5 dB NF," in *IEEE Int. Solid-State Circuits Conf. (ISSCC) Dig. Tech. Papers*, Session 12, Feb. 2009, pp. 222-224.